

From light to baryonic mass: the effect of the stellar mass–to–light ratio on the Baryonic Tully–Fisher relation

Anastasia A. Ponomareva^{1,2*}, Marc A. W. Verheijen^{2,3}, Emmanouil Papastergis^{2,5}, Albert Bosma⁴ and Reynier F. Peletier²

¹*Research School of Astronomy & Astrophysics, Australian National University, Canberra, ACT 2611, Australia*

²*Kapteyn Astronomical Institute, University of Groningen, Postbus 800, NL-9700 AV Groningen, The Netherlands*

³*National Centre for Radio Astrophysics, Tata Institute of Fundamental Research, Postbag 3, Ganeshkhind, Pune 411 007, India*

⁴*Aix Marseille Univ, CNRS, LAM, Laboratoire d’Astrophysique de Marseille, Marseille, France*

⁵*Credit Risk Modeling Department, Coöperative Rabobank U.A., Croeselaan 18, Utrecht NL-3521CB, The Netherlands*

11 December 2017

ABSTRACT

In this paper we investigate the statistical properties of the Baryonic Tully-Fisher relation (BTFR) for a sample of 32 galaxies with accurate distances based on Cepheids and/or TRGB stars. We make use of homogeneously analysed photometry in 18 bands ranging from the FUV to 160 μm , allowing us to investigate the effect of the inferred stellar mass–to–light ratio (Υ_*) on the statistical properties of the BTFR. Stellar masses of our sample galaxies are derived with four different methods based on full SED-fitting, studies of stellar dynamics, near-infrared colours, and the assumption of the same $\Upsilon_*^{[3.6]}$ for all galaxies. In addition, we use high-quality, resolved HI kinematics to study the BTFR based on three kinematic measures: W_{50}^i from the global HI profile, and V_{max} and V_{flat} from the rotation curve. We find the intrinsic perpendicular scatter, or tightness, of our BTFR to be $\sigma_{\perp} = 0.026 \pm 0.013$ dex, consistent with the intrinsic tightness of the 3.6 μm luminosity-based TFR. However, we find the slope of the BTFR to be 2.99 ± 0.2 instead of 3.7 ± 0.1 for the luminosity-based TFR at 3.6 μm . We use our BTFR to place important observational constraints on theoretical models of galaxy formation and evolution by making comparisons with theoretical predictions based on either the Λ CDM framework or modified Newtonian dynamics.

Key words: galaxies: fundamental parameters – galaxies: kinematics, dynamics, photometry, scaling relations

1 INTRODUCTION

The empirical scaling relations of galaxies are a clear demonstration of the underlying physical processes that govern the formation and evolution of galaxies. Any particular theory of galaxy formation and evolution should therefore explain their origin and intrinsic properties such as their slope, scatter and zero point. One of the most multifunctional and well-studied empirical scaling relations is the relation between the width of the neutral hydrogen line and the luminosity of a galaxy (Tully & Fisher 1977), known as the Tully-Fisher relation (TFR). Originally established as a tool to measure distances to galaxies, it became one of the most widely used relations to constrain theories of galaxy forma-

tion and evolution (Navarro & Steinmetz 2000; Vogelsberger et al. 2014; Schaye et al. 2015; Verbeke et al. 2015; Macciò et al. 2016). Even though the TFR has been extensively studied and explored during the past four decades (Verheijen 2001; McGaugh 2005; Tully & Courtois 2012; Sorce et al. 2013; Karachentsev et al. 2017), many open questions still remain, especially those relating to the physical origin and the underlying physical mechanisms which maintain the TFR as galaxies evolve (McGaugh & de Blok 1998; Courteau & Rix 1999; van den Bosch 2000). Finding answers to these questions is crucial for our comprehension of galaxies and how they form and evolve.

At present, the physical principle behind the TFR is widely considered to be a relation between the baryonic mass of a galaxy and the mass of its host dark matter (DM) halo (Milgrom & Braun 1988; Freeman 1999; McGaugh 2005)

* E-mail: anastasia.ponomareva@anu.edu.au

since the TFR links the baryonic content of a galaxy (characterised by its luminosity) to a dynamical property (characterised by its rotational velocity). Therefore, if a galaxy’s luminosity is a proxy for a certain baryonic mass fraction, a relation between its rotational velocity and its total baryonic mass should exist. Indeed, [McGaugh et al. \(2000\)](#) have shown the presence of such a relation, which is now widely known as the Baryonic Tully-Fisher relation (BTFR).

Subsequently, the BTFR was widely studied ([Bell & de Jong 2001](#); [Zaritsky et al. 2014](#); [Papastergis et al. 2016](#); [Lelli et al. 2016](#)) as it has a great potential to put quantitative constraints on models of galaxy formation and evolution. Moreover, it clearly offers some challenges to the Λ CDM cosmology model. Foremost, it follows just a single power-law over a broad range of galaxy masses. This is contrary to the expected relation in the Λ CDM paradigm of galaxy formation, where the BTFR “curves” at the low velocity range ([Trujillo-Gomez et al. 2011](#); [Desmond 2012](#)). Second, the BTFR appears to be extremely tight, suggesting a zero intrinsic scatter ([Verheijen 2001](#); [McGaugh 2012](#)). It is difficult to explain such a small observational scatter in the BTFR, as various theoretical prescriptions in simulations, such as the mass–concentration relation of dark matter halos or the baryon–to–halo mass ratio, result in a significant scatter. For instance, [Lelli et al. \(2016\)](#) have found an intrinsic scatter of ~ 0.1 dex, while [Dutton \(2012\)](#) predicts a minimum intrinsic scatter of ~ 0.15 dex, using a semi-analytic galaxy formation model in the Λ CDM context. However, [Papastergis et al. \(2016\)](#) have shown that theoretical results seem to reproduce the observed BTFR better if hydrodynamic simulations are considered instead of semi-analytical models ([Governato et al. 2012](#); [Brooks & Zolotov 2014](#); [Christensen et al. 2014](#)). This suggests that the galactic properties that are expected to contribute to the intrinsic scatter (halo spin, halo concentration, baryon fraction) are not completely independent from each other. Moreover, the BTFR is also used to test alternative theories of gravity, and various studies argue that the observed properties of the BTFR can be better explained by a modification of the gravity law (e.g. MOND, [Milgrom 1983](#)) than by a theory in which the dynamical mass of galaxies is dominated by the DM, such as in the Λ CDM scenario.

The BTFR can be considered as a reliable tool to test galaxy formation and evolution models only if the statistical properties of the BTFR compared between observations and simulations are as consistent as possible. So far, various observational results differ in details, even though they find similar results in general. For instance, the slope of the observed relation varies from ~ 3.5 ([Bell & de Jong 2001](#); [Zaritsky et al. 2014](#)) to ~ 4.0 ([McGaugh et al. 2000](#); [Papastergis et al. 2016](#); [Lelli et al. 2016](#)). Therefore, it is important to address the observational limitations when studying the BTFR because the measurements of the rotational velocity and of the baryonic mass of galaxies are rather difficult. The baryonic mass of a galaxy is usually measured as the sum of the stellar and neutral gas components. According to [Bland-Hawthorn & Gerhard \(2016\)](#), the contribution of the hot halo gas is larger in mass, but this is usually not accounted for in the BTFR. Since the neutral atomic gas mass can be measured straightforwardly from 21-cm line observations while the contribution of molecular gas to the total baryonic mass is often small, the biggest contributor

to the uncertainty in the BTFR is the stellar mass measurement. Even though various prescriptions to determine the stellar mass are available, the relative uncertainty in the stellar mass derived from photometric imaging usually ranges between 60–100 % ([Pforr et al. 2012](#)). Moreover, various recipes for deriving the stellar mass-to-light ratio (Υ_*) from spectro–photometric measurements depend on a number of parameters, such as the adopted initial stellar mass function (IMF), the star formation history (SFH) and uncertainties in modelling the advanced phases of stellar evolution, such as AGB stars ([Maraston et al. 2006](#); [Conroy et al. 2009](#)). There are alternative ways to measure the stellar mass of galaxies, for example by estimating it from the vertical velocity dispersion of stars in nearby face-on disk galaxies ([Bershadsky et al. 2010](#)). However, such methods are observationally expensive and have systematic limitations as well ([Aniyan et al. 2016](#)).

The BTFR requires an accurate measurement of the rotational velocity of galaxies. There are several methods to estimate this parameter, derived either from the width of the global HI profile or from spatially resolved HI kinematics. It was shown by [Verheijen \(2001\)](#) that the scatter in the luminosity–based TFR can be decreased if the velocity of the outer flat part (V_{flat}) of the rotation curve is used as a measure of the rotational velocity, instead of the corrected width of the global HI profile W_{50}^z . As was shown in [Ponomareva et al. 2016](#) (hereafter [P16](#)), the rotational velocity derived from the width of the global HI profile may differ from the value measured from the flat part of the rotation curve, especially for galaxies which have either rising or declining rotation curves. These issues should be considered when studying the statistical properties of the BTFR. Likewise, [Brook et al. \(2016\)](#) demonstrated with a set of simulated galaxies that the statistical properties of the BTFR vary significantly, depending on the rotational velocity measure used.

In order to take into account the uncertainties mentioned above and to establish a more definitive study of the BTFR, we consider in detail four methods to estimate the stellar mass of galaxies. This allows us to study the dependence of the statistical properties of the BTFR as a function of the method used to determine the stellar mass: full SED–fitting, dynamical Υ_* calibration, $\Upsilon_*^{[3.6]}$ as a function of [3.6]–[4.5] colour and constant $\Upsilon_*^{[3.6]}$. Furthermore, we consider the BTFR based on three velocity measures: W_{50} from the corrected width of the global HI profile, and V_{flat} and V_{max} from the rotation curve. This allows us to study how the slope, scatter and tightness of the BTFR change if the relation is based on a different definition of the rotational velocity.

This paper is organised as follows: Section 2 describes the sample of BTFR galaxies. Section 3 describes the data sources. Section 4 describes the gas mass derivation. Section 5 describes four methods to estimate the stellar mass of the sample galaxies. Section 6 provides the comparison of the BTFRs based on different stellar mass measurements. Section 7 presents our adopted BTFR. Section 8 demonstrates the comparison of our adopted BTFR with previous observational studies and theoretical results. Section 9 presents concluding remarks.

2 THE SAMPLE

In order to study the statistical properties of the BTFR and to be able to compare our results with the luminosity-based TFR studied in Ponomareva et al. 2017 (hereafter P17), we adopt the same sample of 32 galaxies used in P17. These galaxies were selected according to the following criteria: 1) Sa or later in morphological type, 2) an inclination above 45° , 3) HI profiles with adequate S/N and without obvious distortions or contributions from possible companions to the flux. The main properties of the sample are summarised in Table 1 in P16. This sample has been specifically selected to study the BTFR in detail and has properties that help minimize many of the observational uncertainties involved in the measurement of the relation such as: 1) poorly known distances, 2) the conversion of light into stellar mass, and 3) the lack of high-quality HI rotation curves.

First, galaxies in our sample have accurate primary distance measurements, either from the Cepheid period–luminosity relation (Freedman et al. 2001) or/and from the brightness of the tip of the red giant branch (Rizzi et al. 2007). If simple Hubble flow distances were used for the nearby galaxies in our sample, the distance uncertainties might contribute up to 0.4 mag to the observed scatter of the luminosity-based TFR. In contrast, the distance uncertainty contribution to the observed scatter in the TFR is only 0.07 mag if independently measured distances are adopted (P17). Second, our adopted sample benefits from homogeneously analysed photometry in 18 bands, ranging from FUV to $160 \mu\text{m}$. This allows us to perform a spectral energy distribution (SED) fitting to derive the stellar masses based on stellar population modelling. Third, all galaxies from our sample have HI synthesis imaging data and high-quality rotation curves available, from which we derive the maximum rotational velocity V_{max} and the outer flat rotational velocity V_{flat} (P16).

3 DATA SOURCES

To derive the main ingredients for the BTFR such as stellar masses, molecular and atomic gas masses and rotational velocities, we use the following data sources and techniques.

3.1 21-cm aperture synthesis imaging

For our study we collected 21-cm aperture synthesis imaging data from the literature, since many of our galaxies were already observed as part of several large HI surveys (see P16 for an overview). Moreover, we observed ourselves three more galaxies with the GMRT (see P16 for more details). All data cubes were analysed in the same manner and various data products were derived, including global HI profiles, surface density profiles and high-quality rotation curves. Based on these homogeneous HI data products, we have measured rotational velocities in three ways: from the corrected width of the global HI profile ($V_{circ} = W_{50}^{R,t,i}/2$), as the maximal rotational velocity (V_{max}) from the rotation curve, and as the velocity of the outer “flat” part of the rotation curve (V_{flat}), noting that massive and compact galaxies often show a declining rotation curve in their inner regions where $V_{max} > V_{flat}$.

3.2 Photometry

In P17 we have derived the main photometric properties of our sample galaxies to study the wavelength dependence of the slope, scatter and tightness of the luminosity-based TFR in 12 photometric bands from FUV to $4.5 \mu\text{m}$ with magnitudes corrected for internal and Galactic extinction. For this work, we have collected and analysed supplementary Wide-field Infrared Survey Explorer (WISE, Wright et al. 2010) imaging data at $12 \mu\text{m}$ and $22 \mu\text{m}$. In each pass-band, we calculate magnitudes in apertures of increasing area and extrapolate the resulting surface brightness profiles to obtain the total magnitudes. Moreover, to determine the far-infrared emission we collected from the literature far-infrared fluxes at $60 \mu\text{m}$ and $100 \mu\text{m}$ as measured by IRAS, and at $70 \mu\text{m}$ and $160 \mu\text{m}$ as measured with Herschel/MIPS. We use these photometric measurements to estimate the stellar masses of our sample galaxies.

4 GAS MASS

Gas is an important contributor to the baryonic mass of a spiral galaxy and plays a crucial role in the study of the BTFR. For instance, when assuming the same stellar mass-to-light ratio for all sample galaxies, only the gas mass is responsible for any difference in the slope and tightness of the BTFR compared to the luminosity-based TFR.

The HI mass can be directly measured from the 21-cm radio observations, while the H_2 mass can only be obtained indirectly using either CO or warm dust observations (Leroy et al. 2009; Westfall et al. 2011; Martinsson et al. 2013). Although generally the atomic gas mass dominates over the molecular component, there are several known cases where the estimated mass of the molecular gas is similar to, or exceeds, the mass of the atomic gas (Leroy et al. 2009; Saintonge et al. 2011; Martinsson et al. 2013). Therefore, it is important to take both constituents into account when studying the BTFR. In this section we describe how the masses of the atomic and molecular gas were derived.

4.1 HI mass

We calculate the HI masses of our sample galaxies using the integrated HI-line flux density ($\int S_\nu dv$ [Jy kms^{-1}]) derived as part of the analysis of the 21-cm radio synthesis imaging observations (P16), according to:

$$M_{HI} [M_\odot] = 2.36 \times 10^5 \times D^2 [\text{Mpc}] \int S_\nu dv [\text{Jy kms}^{-1}], \quad (1)$$

where D is the distance to the galaxy, as listed in P16, Table 1. We derive the error on the HI mass by following a full error propagation calculation, taking into account the measurement error on the flux density and the error on the distance modulus as calculated in P16. Furthermore, we calculate the total neutral atomic gas mass as

$$M_{atom} = 1.4 \times M_{HI}, \quad (2)$$

where the factor 1.4 accounts for the primordial abundance of helium and metals. The mass of the neutral atomic gas component is listed in Table 2. It is important to note that

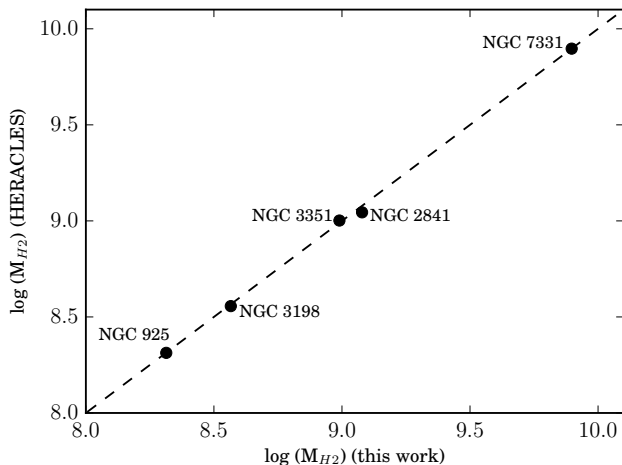


Figure 1. The comparison between the H_2 mass derived using the $22\ \mu\text{m}$ surface brightness (this work), and the H_2 mass derived from direct CO measurements from the HERACLES survey (Leroy et al. 2009). The dashed line represents the 1:1 correspondence.

we estimate the $H\text{I}$ mass under the assumption that all of the 21 cm emission is optically thin, which is not always the case and up to 30% of the $H\text{I}$ mass can be hidden due to $H\text{I}$ self-absorption according to Peters et al. (2017).

4.2 H_2 mass

Unfortunately, the distribution of the molecular hydrogen (H_2) in galaxies can not be directly observed. Therefore, indirect methods are required to estimate the mass of the H_2 (M_{H_2}). The most straightforward and widely studied tracer of the H_2 gas is the CO emission line, which can be directly observed (Leroy et al. 2009; Saintonge et al. 2011; Young & Scoville 1991). The M_{H_2} can be estimated using the $^{12}CO(J=1\rightarrow 0)$ flux ($I_{CO}\Delta V$) and the $^{12}CO(J=1\rightarrow 0)$ -to- H_2 conversion factor X_{CO} . However, only 5 out of 32 galaxies in our sample have CO measurements available. In order to ensure a homogeneous analysis, we use instead the $22\ \mu\text{m}$ imaging photometry to estimate the CO column-density distribution. This approach is motivated by various studies that demonstrate a tight correlation between the infrared luminosity of spiral galaxies, associated with the thermal dust emission, and their molecular gas content as traced by the CO emission (Westfall et al. 2011; Bendo et al. 2007; Paladino et al. 2006; Young & Scoville 1991). For our study we use the following relation from Westfall et al. (2011) to derive $I_{CO}\Delta V$:

$$\log(I_{CO}\Delta V) = 1.08 \cdot \log(I_{22\mu\text{m}}) + 0.15, \quad (3)$$

where $I_{CO}\Delta V$ is in K km s^{-1} and $I_{22\mu\text{m}}$ is the $22\ \mu\text{m}$ surface brightness in MJy sr^{-1} . Note that Westfall et al. (2011) used $24\ \mu\text{m}$ fluxes in their study. However, the $24\ \mu\text{m}$ and $22\ \mu\text{m}$ bands are very similar and therefore we proceed our study using the $22\ \mu\text{m}$ flux. We do not detect $22\ \mu\text{m}$ flux emission in only 2 galaxies, NGC 3319 and NGC 4244, which is not surprising as these two galaxies are dwarfs. In dwarf galaxies,

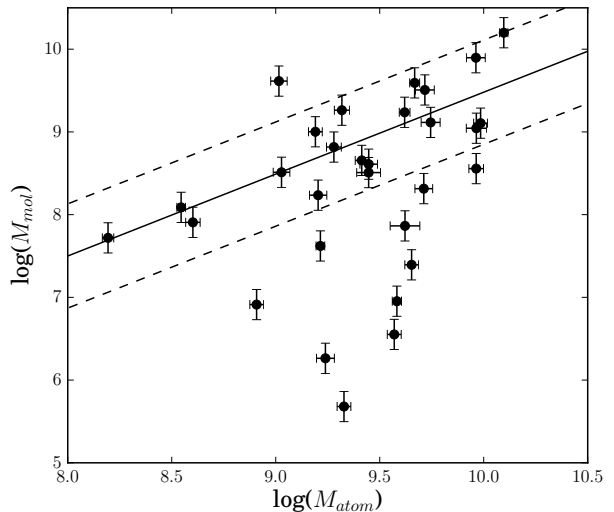


Figure 2. M_{atom} vs. M_{mol} for our sample galaxies. The solid line indicates the fit from Saintonge et al. (2011). The dashed lines represent the scatter in the $M_{atom} - M_{mol}$ relation ($\sigma = 0.41$ dex) also from Saintonge et al. (2011). Note that only 30 galaxies are shown, as we did not detect NGC 3319 and NGC 4244 at $22\ \mu\text{m}$.

the low metallicities cause large uncertainties in the X_{CO} factor, which makes it impossible to relate the amount of CO to H_2 . Of course, H_2 is strongly correlated with the SFR, which is very low in dwarf galaxies, and therefore one can conclude that the contribution of H_2 to the bulk mass of a dwarf galaxy is negligible. Next, we calculate the M_{H_2} using the X_{CO} conversion factor (Westfall et al. 2011; Martinsson et al. 2013):

$$\Sigma M_{H_2} [M_{\odot} \text{pc}^{-2}] = 1.6 I_{CO} \Delta V \times X_{CO} \cdot \cos(i), \quad (4)$$

where i is the inclination angle as derived from the $H\text{I}$ kinematics. Even though the use of X_{CO} is a standard procedure to convert CO column density into molecular hydrogen gas mass, different studies offer various derivations of X_{CO} . Here, we adopt $X_{CO} = 2.7(\pm 0.9) \times 10^{20} \text{cm}^{-2} (\text{K km s}^{-1})^{-1}$ from Westfall et al. (2011). In that study, they use a mean value of the Galactic measurement of X_{CO} from Dame et al. (2001) and the measurements for M31 and M33 from Bolatto et al. (2008). In Figure 1 we compare our H_2 masses with those derived from the direct CO measurements from the HERACLES survey (Leroy et al. 2009) for five galaxies in our sample. It is clear that our estimates are in good agreement. To account for the mass of helium and heavier elements corresponding to hydrogen in the molecular phase, we calculate the mass of the molecular gas component as:

$$M_{mol} = 1.4 \times M_{H_2}. \quad (5)$$

Despite a good agreement with the HERACLES measurements, the method to estimate the CO column density from the $22\ \mu\text{m}$ surface brightness has its limitations which result in a significant estimated error on the molecular gas mass of $\sim 42\%$ (Westfall et al. 2011; Martinsson et al. 2013), which we adopted for our measurements.

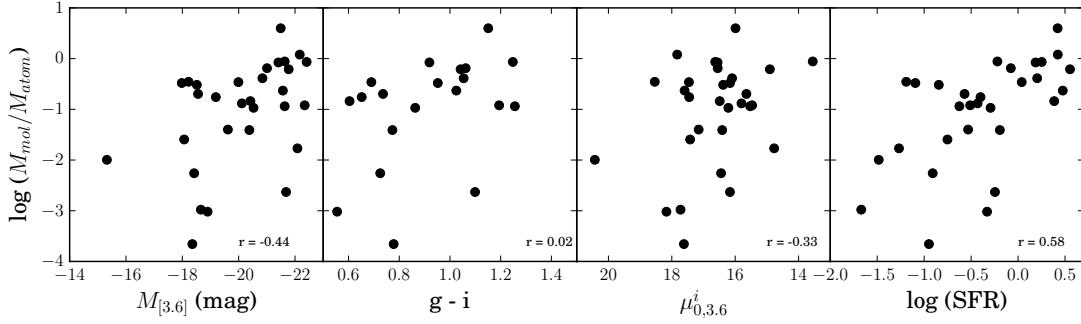


Figure 3. Correlations between R_{mol} and global galaxy properties. In the bottom right corner the Pearson’s correlation coefficients are shown.

4.3 M_{atom} vs. M_{mol}

Presuming that the molecular gas forms out of collapsing clouds of atomic gas, it seems reasonable to expect a tight correlation between the masses of the atomic and molecular components. However, recent studies of the gas content of large galaxy samples have shown that this is not the case. A large scatter is present in the $M_{atom}-M_{mol}$ relation (Leroy et al. 2009; Saintonge et al. 2011; Martinsson et al. 2013). Figure 2 shows the $M_{atom}-M_{mol}$ relation for our sample galaxies. Even though the majority of our galaxies follows the relation from Saintonge et al. (2011) with a similar scatter, we have some outliers with smaller molecular-to-atomic mass ratio ($R_{mol} = M_{mol}/M_{atom}$) which lie below the bottom dashed line in Figure 2.

In Figure 3 we present correlations between R_{mol} and global galaxy properties such as absolute magnitude, colour, central surface brightness and star formation rate. Even though there are some hints that more luminous, redder galaxies with a higher star formation rate tend to have a larger fraction of M_{mol} , the scatter in these correlations is very large, with the best correlation between $\log R_{mol}$ vs SFR. In general, R_{mol} for individual galaxies ranges greatly from 0.001 to 3.97 with a mean value of $\langle R_{mol} \rangle = 0.38$, which is in good agreement with previous studies (Leroy et al. 2009; Saintonge et al. 2011; Martinsson et al. 2013). We find one extreme case, NGC 3627, with $R_{mol} = 3.97$, comparable to UGC 463 with $R_{mol} = 2.98$ (Martinsson et al. 2013), NGC 4736 with $R_{mol} = 1.13$ (Leroy et al. 2009) and G38462 with $R_{mol} = 4.09$ (Saintonge et al. 2011).

It is important to mention that in this section we deliberately do not compare masses of the gaseous components with the estimated masses of the stars in our sample galaxies, because the measurement of the stellar masses is not straightforward and the contribution of the stellar mass to the baryonic mass budget can vary, depending on the method used to estimate stellar masses. We discuss this subject in the following section.

5 STELLAR MASSES

The stellar masses of galaxies, unlike the light, can not be measured directly and, therefore, their estimation is a very complex process with various assumptions and uncertainties. The most common method of estimating the stellar mass

of a galaxy is to convert the measured light into mass using a relevant mass-to-light ratio. However, deciding which mass-to-light ratio to use is not straightforward. It can be derived either from stellar population synthesis models or by measuring the dynamical mass (surface) density of a galaxy. Every method of estimating the mass-to-light ratio has its uncertainties and limitations. In this paper we consider four different methods of estimating the stellar masses, and work out for each of them their effect on the statistical properties of the BTFR. In our study, regardless of the method, we limit ourselves to integral mass-to-light ratios, i.e. no radial variation of this quantity is analysed. Even though bulges are expected to have higher mass-to-light ratios than disks, we justify this approach given the absence of strong colour gradients with radius and the small number of bulge dominated galaxies in our sample.

5.1 SED modeling

The light that comes from stars of different ages and masses dominates the flux in different photometric bands. Thus, for example, young hot stars dominate the flux in the UV bands while old stellar populations are more dominant in the infrared bands: e.g. $0.8-5 \mu\text{m}$. Moreover, mid- and far-infrared bands can trace the galactic dust at various temperatures. The differences between magnitudes in these photometric bands (galactic colours) contain information on various properties of the stars in a galaxy such as their age or metallicity. Therefore, stellar population models aim to create a mix of stellar populations that is able to simultaneously reproduce a wide range of observed colours. Hence, modelling of the spectral energy distribution allows us to estimate the total stellar mass of the composite stellar population. This process is called spectral energy distribution (SED) fitting.

It is important to measure the luminosity of a galaxy at as many wavelengths as possible in order to provide more constraints on the various physical parameters of a model. Having photometric measurements in many bands, spanning from the far-ultraviolet to the far-infrared, helps to derive more reliable values for various galactic properties that influence the estimation of the stellar mass (e.g., star formation history, metallicity). However, it should be kept in mind that stellar mass estimates from SED-fitting are nonetheless limited by systematic uncertainties in the theoretical mod-

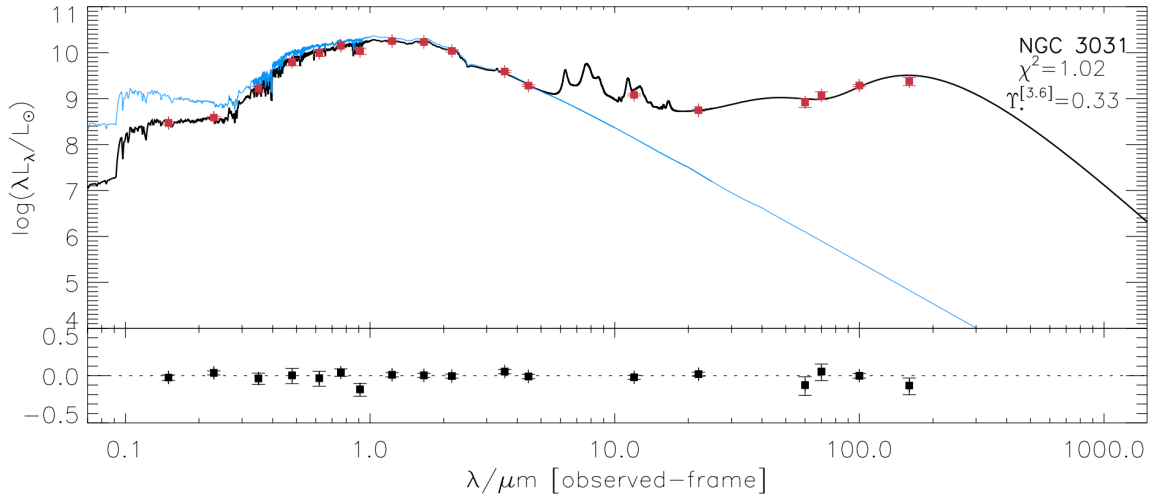


Figure 4. An example of the best-fit model, performed with MAGPHYS (in black) over the observed spectral energy distribution of NGC 3031. The blue curve shows the unattenuated stellar population spectrum. The bottom plot shows the residuals for each measurement $((L_{obs} - L_{mod})/L_{obs})$.

elling of stellar populations. For example, limited knowledge regarding the initial mass function (IMF), uncertainties in the theoretical modelling of advanced stages of stellar evolution, or limitations of stellar spectral libraries cannot be suppressed with better photometric data.

To calculate the stellar masses of our sample galaxies using SED-fitting, we derived fluxes in 14 photometric bands from FUV to $22 \mu\text{m}$. Moreover, we collected from the literature far-infrared fluxes at $60 \mu\text{m}$ and $100 \mu\text{m}$ as measured by IRAS, and at $70 \mu\text{m}$ and $160 \mu\text{m}$, as measured with Herschel/MIPS (see Section 3.2). Consequently, we have at our disposal measured fluxes in 18 photometric bands for every galaxy (except for 10 galaxies that lack SDSS data, see P17). We performed the fitting of the spectral energy distribution of every galaxy, using the SED-fitting code “MAGPHYS”, following the approach described in da Cunha et al. (2008). The advantage of this code is its ability to interpret the mid- and far-infrared luminosities of galaxies consistently with the UV, optical and near-infrared luminosities. To interpret stellar evolution it uses the Bruzual & Charlot (2003) stellar population synthesis model. This model predicts the spectral evolution of stellar populations at ages between 1×10^5 and 2×10^{10} yr. In this model, the stellar populations of a galaxy are described with a series of instantaneous bursts, so called “simple stellar populations”. The code adopts the Chabrier (2003) Galactic disk IMF. The code also takes into account a new prescription for the evolution of low and intermediate mass stars on the thermally pulsating asymptotic giant branch (Marigo & Girardi 2007). This prescription helps to improve the prediction of the near-infrared colours of an intermediate age stellar population, which is important in the context of spiral galaxies. To describe the attenuation of the stellar light by the dust, the code uses the two-component model of Charlot & Fall (2000). It calculates the emission from the dust in giant molecular clouds and in the diffuse ISM, and then distributes the luminosity over wavelengths to compute the infrared spectral energy distribution. The

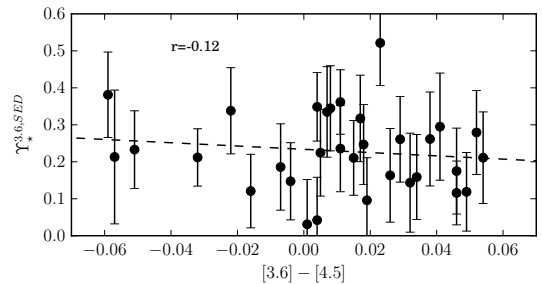


Figure 5. Derived stellar mass-to-light ratios from the SED-fitting ($\Upsilon_{\star}^{SED,[3.6]}$) as a function of the $[3.6] - [4.5]$ colour. The linear fit is shown with the dashed line, r is Pearson’s correlation coefficient.

ability of the SED-fitting code to take a dusty component into account while performing the stellar mass estimate is very important for our study because we deal with star forming spirals in which the amount of dust and obscuration is not negligible. From the SED fitting we derive a stellar mass estimate for each galaxy in our sample. As an example, the best-fit SED model for NGC 3031 is shown in Figure 4 (see Appendix B for the SED fits of other sample galaxies).

Thereby we obtain the stellar mass-to-light ratio (Υ_{\star}) for the light in several photometric bands. We present the Υ_{\star} for the K and $3.6 \mu\text{m}$ bands in Table 1 together with the other parameters obtained from the SED modelling. Notably, we will refer to the stellar mass-to-light ratio, measured from the SED-fitting as $\Upsilon_{\star}^{SED,\lambda}$, where λ is a particular photometric band. Interestingly, we do not find any correlation between $\Upsilon_{\star}^{SED,[3.6]}$ and the $[3.6] - [4.5]$ colour (Figure 5), while such a correlation exists in case $\Upsilon_{\star}^{[3.6]}$ is measured with other methods (see below).

We assign a relative error to the SED-based stellar mass-to-light ratio ($\Upsilon_{\star}^{SED,\lambda}$) equal to $\epsilon_{\Upsilon_{\star}^{SED,\lambda}} = 0.1$ dex

| name | log(sSFR) | log(SFR) | log(M_{\star}^{SED}) | log(M_{dust}) | $\Upsilon_{\star}^{SED,[3.6]}$ | $\Upsilon_{\star}^{SED,K}$ |
|----------|-----------|----------|--------------------------|-------------------|--------------------------------|----------------------------|
| NGC 55 | -11.60 | -2.40 | 9.20 | 6.27 | 0.32 | 0.34 |
| NGC 224 | -15.37 | -4.79 | 10.57 | 7.16 | 0.21 | — |
| NGC 247 | -10.55 | -1.51 | 9.04 | 6.68 | 0.15 | 0.21 |
| NGC 253 | -13.06 | -2.64 | 10.41 | 8.03 | 0.22 | 0.32 |
| NGC 300 | -10.57 | -1.66 | 8.91 | 6.58 | 0.19 | 0.21 |
| NGC 925 | -12.18 | -2.38 | 9.80 | 7.08 | 0.35 | 0.41 |
| NGC 1365 | -13.18 | -2.38 | 10.80 | 7.56 | 0.33 | 0.38 |
| NGC 2366 | -7.81 | -0.65 | 7.16 | 4.57 | 0.04 | 0.04 |
| NGC 2403 | -10.77 | -1.61 | 9.16 | 6.86 | 0.12 | 0.17 |
| NGC 2541 | -10.89 | -1.90 | 8.99 | 6.09 | 0.16 | 0.23 |
| NGC 2841 | -14.36 | -3.69 | 10.67 | 8.05 | 0.21 | 0.27 |
| NGC 2976 | -10.79 | -1.94 | 8.84 | 6.07 | 0.17 | 0.24 |
| NGC 3031 | -13.97 | -3.38 | 10.59 | 7.70 | 0.33 | 0.45 |
| NGC 3109 | -9.27 | -1.62 | 7.65 | 4.71 | 0.14 | 0.19 |
| NGC 3198 | -11.83 | -1.94 | 9.89 | 7.56 | 0.21 | 0.27 |
| IC 2574 | -8.30 | -0.58 | 7.72 | 5.63 | 0.03 | 0.06 |
| NGC 3319 | -11.33 | -1.99 | 9.34 | 6.28 | 0.24 | 0.26 |
| NGC 3351 | -12.75 | -2.40 | 10.35 | 7.34 | 0.34 | 0.40 |
| NGC 3370 | -10.73 | -1.17 | 9.56 | 7.25 | 0.10 | 0.14 |
| NGC 3621 | -12.18 | -2.25 | 9.93 | 7.47 | 0.30 | 0.40 |
| NGC 3627 | -11.99 | -1.79 | 10.21 | 7.93 | 0.16 | 0.20 |
| NGC 4244 | -10.62 | -1.79 | 8.83 | 5.95 | 0.12 | 0.18 |
| NGC 4258 | -12.77 | -2.40 | 10.37 | 7.24 | 0.21 | 0.26 |
| NGC 4414 | -12.52 | -1.98 | 10.54 | 8.21 | 0.26 | 0.31 |
| NGC 4535 | -12.50 | -2.13 | 10.37 | 7.74 | 0.25 | 0.30 |
| NGC 4536 | -12.25 | -2.06 | 10.19 | 7.86 | 0.28 | 0.41 |
| NGC 4605 | -11.07 | -1.82 | 9.25 | 6.64 | 0.26 | 0.36 |
| NGC 4639 | -12.51 | -2.36 | 10.15 | 7.18 | 0.34 | 0.41 |
| NGC 4725 | -13.57 | -2.91 | 10.66 | 7.66 | 0.38 | 0.41 |
| NGC 5584 | -10.93 | -1.46 | 9.47 | 6.54 | 0.12 | 0.12 |
| NGC 7331 | -13.93 | -2.84 | 11.09 | 8.20 | 0.52 | 0.68 |
| NGC 7793 | -11.64 | -2.27 | 9.37 | 6.38 | 0.36 | 0.44 |

Table 1. Results of the SED-fitting performed with MAGPHYS. Column (1): name; Column (2): log of the specific star formation rate; Column (3): log of the star formation rate; Column (4): log of the stellar mass; Column (5): log of the dust mass; Column (6): stellar mass-to-light ratio for the stellar masses from Column (4) and light in the $3.6\mu\text{m}$ band; Column (7): stellar mass-to-light ratio for the stellar masses from Column (4) and light in the K- band;

motivated by the test by [Roediger & Courteau \(2015\)](#), who performed SED-fitting with “MAGPHYS” on a sample of mock galaxies. They could recover the known stellar masses with a scatter of 0.1 dex for various samples using a different number of observational bands. Finally, we calculate a fractional error on the stellar mass as follows:

$$\epsilon_{M_{\star}^{SED}}^2 = (10^{\epsilon_m/2.5} - 1)^2 + \epsilon_{\Upsilon_{\star}}^2, \quad (6)$$

where ϵ_m is the mean error in the absolute magnitude over all bands, equal to $\epsilon_m = 0.15$ mag. Note that the distance uncertainty is already included in this error on the magnitude. The global parameters of our sample galaxies based on the SED-fitting method are summarised in Table 1.

5.2 Dynamical Υ_{\star} calibration

Another method to estimate the stellar masses of spiral galaxies is by measuring the mass surface density of their disks dynamically. The strategy for disk galaxies is to measure the vertical stellar velocity dispersion (σ_z), which can

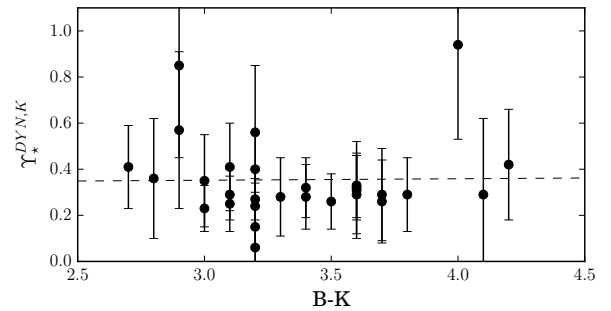


Figure 6. Stellar mass-to-light ratios from the DMS ($\Upsilon_{\star}^{Dyn,K}$) as a function of the B-K colour.

be used to obtain the dynamical mass surface density of a collisionless stellar disk in equilibrium:

$$\Sigma_{dyn} = \frac{\sigma_z^2}{\pi G \kappa h_z \mu}, \quad (7)$$

where μ is the surface brightness, G is the gravitational constant, h_z is the disk scale height and κ is the vertical mass distribution parameter ([van der Kruit & Searle 1981](#); [Bahcall & Casertano 1984](#)). While μ can be easily measured from

photometric studies, and there is a well-calibrated relation between the disk scale length h_r and disk scale height h_z (de Grijs & van der Kruit 1996; Kregel et al. 2002), σ_z is very difficult to measure. Here, we take advantage of the DiskMass Survey (DMS) (Bershady et al. 2010) for dynamically calibrated stellar mass-to-light ratios, which were obtained by measuring σ_z for a sample of 30 spiral galaxies (Martinsson et al. 2013). The DMS sample is mostly *Sc* spirals and does not overlap with our BTFR sample. In that study the line-of-sight stellar velocity dispersion (σ_{LOS}) was measured and then converted into σ_z . To minimize errors on σ_z , which significantly affect Σ_{dyn} , spiral galaxies close to face-on were observed. Consequently, the stellar mass surface density was calculated following:

$$\Sigma_{\star} = \Sigma_{dyn} - \Sigma_{mol} - \Sigma_{atom}, \quad (8)$$

where Σ_{mol} and Σ_{atom} are the mass surface densities of the molecular and atomic hydrogen, see Section 4. Then, the stellar mass-to-light ratio Υ_{\star} can be expressed as follows:

$$\Upsilon_{\star} = \frac{\Sigma_{\star}}{\mu}, \quad (9)$$

where μ is the K-band surface brightness (Martinsson et al. 2013). We refer to this stellar mass-to-light ratio as $\Upsilon_{\star}^{Dyn,K}$.

Next, we use $\Upsilon_{\star}^{Dyn,K}$ from the DMS and check if those values correlate with a colour term, which can be measured directly from the photometry. If such a correlation exists, we would be able to adopt the $\Upsilon_{\star}^{Dyn,K}$ as a function of colour for our sample. However, we did not find any correlation (see Figure 6). Therefore, we adopt a median value for $\Upsilon_{\star}^{Dyn,K}$ from Martinsson et al. (2013), equal to $\langle \Upsilon_{\star}^{Dyn,K} \rangle = 0.29$ and we apply it to our K-band magnitudes to derive stellar masses for our sample galaxies:

$$M_{\star}^{Dyn} = \langle \Upsilon_{\star}^{Dyn,K} \rangle \cdot L_K(L_{\odot}), \quad (10)$$

where the absolute luminosity of the Sun in the K-band is equal to 3.27 mag. For the error on $\langle \Upsilon_{\star}^{Dyn,K} \rangle$ we adopt the median error from Martinsson et al. (2013) equal to $\epsilon_{\langle \Upsilon_{\star}^{Dyn,K} \rangle} = 0.19$ dex and then we calculate the fractional error on the stellar mass according to Eq. 6. We estimate the error on our magnitudes as the mean error of the K-band apparent magnitude, equal to $\epsilon_m = 0.17$ mag.

5.3 $\Upsilon_{\star}^{[3.6]}$ as a function of [3.6]–[4.5] colour

The flux in the 3.6 μm band is considered a good tracer of the old stellar population of galaxies, which is the main contributor to the total stellar mass, especially in early-type galaxies (ETGs). Therefore, in recent years much attention has been given to finding the best way to convert the 3.6 μm flux into stellar mass (Eskew et al. 2012; Querejeta et al. 2015; Röck et al. 2015; Meidt et al. 2012). Many of these studies found a correlation between $\Upsilon_{\star}^{[3.6]}$ and the [3.6]–[4.5] colour.

For instance, Eskew et al. (2012) used measurements of the resolved Large Magellanic Cloud (LMC) star formation history (SFH) (Harris & Zaritsky 2009) to calibrate $\Upsilon_{\star}^{[3.6]}$ by linking the mass in various regions of the LMC to the 3.6

μm flux. They found that the stellar mass can be traced well by the 3.6 μm flux if a bottom-heavy initial mass function (IMF), such as Salpeter, or heavier was assumed. They estimated the stellar mass-to-light ratio to be $\Upsilon_{\star}^{[3.6]} = 0.54$ with a 30 % uncertainty. Subsequently, they found that $\Upsilon_{\star}^{[3.6]}$ in each region of the LMC correlates with the local [3.6]–[4.5] colour, according to:

$$\log \Upsilon_{\star}^{[3.6]} = -0.74([3.6] - [4.5]) - 0.23. \quad (11)$$

Hence, Eq. 11 can be applied to calculate the stellar masses of our galaxies, if the fluxes at 3.6 μm and 4.5 μm are known.

However, it was demonstrated by Meidt et al. (2012) that the flux in the 3.6 μm band can be contaminated by non-stellar emission from warm dust and from PAHs (Shapiro et al. 2010). Therefore, they applied an Independent Component Analysis (ICA) to separate the 3.6 μm flux into contributions from the old stellar population and from non-stellar sources. Thus, according to Meidt et al. (2014) and Norris et al. (2014), a single $\Upsilon_{\star}^{[3.6]} = 0.6$ can be used to convert the 3.6 μm flux into stellar mass, with an uncertainty of only 0.1 dex, provided the observed flux is corrected for non-stellar contamination. Remarkably, a constant $\Upsilon_{\star}^{[3.6]} = 0.6$ was also found by stellar population synthesis models in the infrared wavelength range (2.5–5 μm), using empirical stellar spectra (Röck et al. 2015). In addition, Querejeta et al. (2015) presented an empirical calibration of $\Upsilon_{\star}^{[3.6]}$ as a function of [3.6]–[4.5] colour for galaxies for which the correction for non-stellar contamination was applied. Thus, they expressed the corrected stellar mass-to-light ratio as

$$\Upsilon_{\star}^{[3.6],corr} = (\Upsilon_{\star}^{[3.6]} = 0.6) \times \frac{F_{[3.6],cor}}{F_{[3.6],uncor}}, \quad (12)$$

where $F_{[3.6],cor}$ is the total 3.6 μm flux corrected for non-stellar contamination and $F_{[3.6],uncor}$ is the observed total flux. Hence, a constant $\Upsilon_{\star}^{[3.6]} = 0.6$ is applicable to observed galaxies without any non-stellar contamination, such as in ETGs, while $\Upsilon_{\star}^{[3.6]}$ will decrease for those galaxies which suffer the most from contamination, such as star-forming spirals. Furthermore, they expressed $\Upsilon_{\star}^{[3.6],corr}$ as a function of the [3.6]–[4.5] colour according to:

$$\log \Upsilon_{\star}^{[3.6],corr} = -0.339(\pm 0.057)([3.6] - [4.5]) - 0.336(\pm 0.002). \quad (13)$$

As shown in P17, the scatter in the luminosity-based TFR can be reduced if the corrected 3.6 μm luminosities are used. Therefore, we prefer Eq. 13 for the calibration of $\Upsilon_{\star}^{[3.6]}$ as a function of [3.6]–[4.5] colour. In the remainder of this text, we refer to this mass-to-light ratio as $\Upsilon_{\star}^{[3.6],corr}$. We assign an error to $\Upsilon_{\star}^{[3.6],corr}$ equal to:

$$\epsilon_{\Upsilon_{\star}^{[3.6],corr}}^2 = \epsilon_{\Upsilon_{\star}^{3.6=0.6}}^2 + \epsilon_{F_{[3.6],cor}/F_{[3.6],uncor}}^2, \quad (14)$$

where $\epsilon_{\Upsilon_{\star}^{3.6=0.6}}$ is equal to 0.1 dex (Meidt et al. 2014) and $\epsilon_{F_{[3.6],cor}/F_{[3.6],uncor}}$ is an averaged error on the flux ratios at 3.6 μm , equal to 0.1 dex. Furthermore, we calculate the fractional error on the stellar mass according to Eq. 6, using the error on the magnitude as the mean error on the 3.6 μm apparent magnitude, equal to $\epsilon_m = 0.08$ mag.

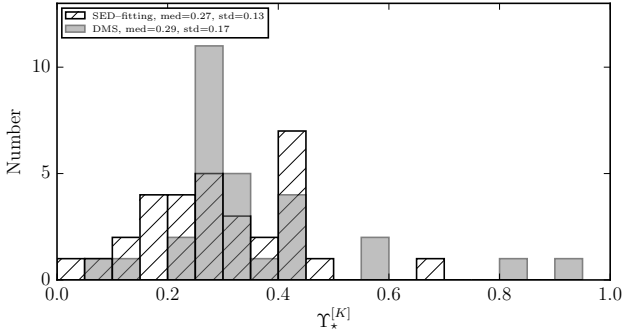


Figure 7. Comparison of the distribution of stellar mass-to-light ratios for the K -band from the DiskMass Survey for a sample of 30 face-on galaxies (dark shade) and from the SED-fitting for our sample (hatched). Distributions have almost the same median with a difference of only 0.02.

5.4 Constant $\Upsilon_*^{[3.6]}$

Despite all previously listed motivations to assign different stellar mass-to-light ratios to disk galaxies, various studies advocate the use of a single mass-to-light ratio for the $3.6 \mu\text{m}$ flux. Different stellar population modelling results estimate $\Upsilon_*^{[3.6]}$ in the range between 0.42 (McGaugh 2012; Schombert & McGaugh 2014) and 0.6 (Röck et al. 2015; Meidt et al. 2014; Norris et al. 2014), pointing out that it is metallicity-dependent. McGaugh et al. (2016) argue that assigning a universal $\Upsilon_*^{[3.6]}$ allows for a direct representation of the data with minimum assumptions, while other methods introduce many more uncertainties.

Furthermore, Lelli et al. (2016) studied the statistical properties of the BTFR with resolved HI kinematics for a different sample of galaxies, using a single value of $\Upsilon_*^{[3.6]} = 0.5$ for the disk component (Schombert & McGaugh 2014). They found an extremely small vertical scatter in the BTFR of $\sigma = 0.1$ dex. This motivated us to adopt a single mass-to-light ratio of $\Upsilon_*^{[3.6]} = 0.5$ as one of the methods for estimating the stellar mass of our sample galaxies. We adopt an error on the stellar mass-to-light ratio equal to $\epsilon_{\Upsilon_*^{[3.6]}=0.5} = 0.07$ dex as reported by Schombert & McGaugh (2014), and calculate the fractional error on the stellar mass according to Eq. 6, with the magnitude error to be the mean error in the $3.6 \mu\text{m}$ apparent magnitudes, equal to $\epsilon_m = 0.08$ mag.

5.5 A comparison between stellar mass-to-light ratios

The four different methods from the previous subsections have demonstrated that stellar masses of spiral galaxies can not be estimated straightforwardly with a single prescription. The resulting stellar masses derived with these different methods are summarised in Table 2. Here we conclude with comparisons between the derived stellar mass-to-light ratios.

We find that the stellar mass-to-light ratios obtained with the SED-fitting cover a wide range of values between 0.04 and 0.67 for the K -band and from 0.03 to 0.52 in the

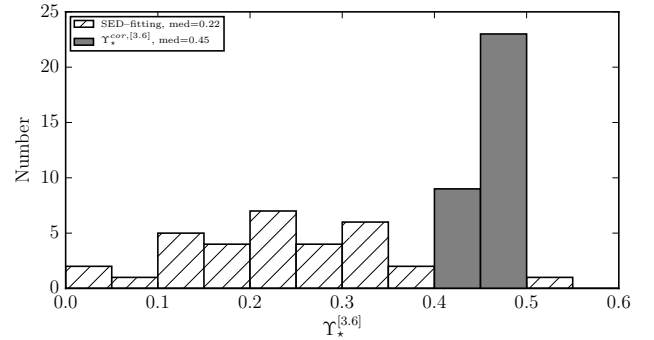


Figure 8. Comparison of the distribution of stellar mass-to-light ratios at $3.6 \mu\text{m}$ as a function of colour (Method 3) in dark shade and from the SED-fitting (Method 1) in hatched area. The distribution of $\Upsilon_*^{SED,[3.6]}$ is much broader than the distribution of $\Upsilon_*^{[3.6],cor}$.

$3.6 \mu\text{m}$ band. Such a large scatter in the bands which are considered to have more or less the same mass-to-light ratio for all galaxies, can be driven by the measurement errors and model uncertainties. Indeed, it is very complicated to assign a single mass-to-light ratio even within a galaxy, as spirals tend to have various components, such as a bulge, disk and spiral arms. Therefore, gradients in the mass-to-light ratio are likely to be present within a galaxy, indicating the differences in IMF and in star formation histories. However, in our analysis we do not consider radial trends in mass-to-light ratios, which may also be a reason for the large scatter and uncertainties in $\Upsilon_*^{SED,K/[3.6]}$. Interestingly, the values of the dynamical mass-to-light ratios in the K -band from the DMS are also spread over a wide range between 0.06 and 0.94.

Figure 7 presents the comparison between the distribution of Υ_*^K from the DMS and from the SED-fitting for different but representative samples of spiral galaxies. Remarkably, these distributions are very similar with a difference in the median of only 0.01, even though the values are measured using different methods for different samples. Furthermore, a comparison between $\Upsilon_*^{SED,[3.6]}$ from the SED-fitting and $\Upsilon_*^{[3.6],cor}$ as a function of the $[3.6]$ – $[4.5]$ colour is shown in Figure 8. While the $\Upsilon_*^{SED,[3.6]}$ is ranging from 0.03 to 0.52, the $\Upsilon_*^{[3.6],cor}$ is spread over a much narrower range from 0.44 to 0.49. The range of $\Upsilon_*^{[3.6],cor}$ is driven by the difference between the uncorrected $3.6 \mu\text{m}$ flux and the flux corrected for non-stellar contamination, which can be significant in spiral galaxies.

6 A COMPARISON OF BARYONIC TULLY-FISHER RELATIONS

In this section we present the BTFRs based on different rotational velocity measures (W_{50} , V_{max} and V_{flat}) and using different stellar mass estimates (see Section 5) in order to study how the slope, scatter and tightness of the BTFR depend on these parameters.

We calculate the baryonic mass of a galaxy as the sum

| Name | $M_{\star,1}$ $10^9 M_{\odot}$ | $M_{\star,2}$ $10^9 M_{\odot}$ | $M_{\star,3}$ $10^9 M_{\odot}$ | $M_{\star,4}$ $10^9 M_{\odot}$ | M_{atom} $10^9 M_{\odot}$ | M_{mol} $10^9 M_{\odot}$ |
|----------------------|-----------------------------------|-----------------------------------|-----------------------------------|-----------------------------------|--------------------------------|-------------------------------|
| NGC 55 | 1.6±0.9 | 1.3±0.8 | 2.2±0.9 | 2.4±1.0 | 1.9±0.01 | 0.17±0.05 |
| NGC 224 ^a | 37.2±14 | – | 83±35 | 87±35 | 5.8±0.68 | 0.10±0.03 |
| NGC 247 | 1.1±0.2 | 1.5±0.9 | 3.4±1.4 | 3.7±1.5 | 2.4±0.17 | 0.002±0.0007 |
| NGC 253 | 26.0±15 | 23±14 | 53±22 | 57±23 | 2.9±0.17 | 2.56±0.76 |
| NGC 300 | 0.8±0.5 | 1.1±0.6 | 2.0±0.8 | 2.1±0.8 | 2.2±0.07 | 0.05±0.01 |
| NGC 925 | 6.3±2.9 | 4.5±2.7 | 8.3±3.5 | 9.0±3.6 | 7.2±0.50 | 0.28±0.08 |
| NGC 1365 | 63.4±36.3 | 49±29 | 86±36 | 94±38 | 17±0.57 | 22.1±6.64 |
| NGC 2366 | 0.01±0.01 | 0.1±0.06 | 0.1±0.06 | 0.1±0.06 | 1.1±0.06 | 0.01±0.00 |
| NGC 2403 | 1.4±0.8 | 2.5±1.5 | 5.4±2.2 | 6.0±2.4 | 3.6±0.18 | 0.63±0.18 |
| NGC 2541 | 1.0±0.5 | 1.2±0.7 | 2.7±1.1 | 2.9±1.2 | 6.3±0.33 | 0.03±0.01 |
| NGC 2841 | 46.8±42.2 | 50±30 | 101±42 | 111±44 | 12±1.02 | 1.55±0.46 |
| NGC 2976 | 0.7±0.4 | 0.8±0.5 | 1.7±0.7 | 1.9±0.8 | 0.2±0.009 | 0.07±0.02 |
| NGC 3031 | 38.5±24.8 | 25±15 | 55±23 | 57±23 | 3.9±0.36 | 0.45±0.13 |
| NGC 3109 | 0.04±0.01 | 0.07±0.04 | 0.1±0.05 | 0.1±0.06 | 0.7±0.05 | 0.01±0.007 |
| NGC 3198 | 7.7±4.6 | 8.3±4.9 | 16±6.8 | 18±7.3 | 12±0.74 | 0.50±0.15 |
| IC 2574 | 0.05±0.02 | 0.2±0.1 | 0.7±0.3 | 0.8±0.3 | 1.9±0.10 | 0.05±0.001 |
| NGC 3319 | 2.2±1.2 | 2.4±1.4 | 4.2±1.7 | 4.6±1.8 | 5.1±0.28 | 0±0 |
| NGC 3351 | 22.4±12.7 | 16±9.7 | 29±12 | 32±13. | 2.1±0.11 | 1.40±0.42 |
| NGC 3370 | 3.6±2.1 | 7.6±4.5 | 17±7.2 | 18±7.6 | 3.9±0.27 | 0.57±0.17 |
| NGC 3621 | 8.4±6.1 | 6.1±3.6 | 12±5.3 | 14±5.7 | 13±0.74 | 1.78±0.53 |
| NGC 3627 | 16.1±9.2 | 24±14 | 45±19 | 50±20 | 1.4±0.09 | 5.76±1.72 |
| NGC 4244 | 0.7±0.3 | 1.1±0.6 | 2.6±1.1 | 2.8±1.1 | 2.9±0.16 | 0±0 |
| NGC 4258 | 23.2±20.8 | 25±15 | 52±22 | 54±22 | 7.7±0.58 | 1.82±0.54 |
| NGC 4414 | 34.4±19.7 | 32±19 | 59±25 | 65±26 | 7.2±0.54 | 4.50±1.35 |
| NGC 4535 | 23.3±17.1 | 23±13 | 42±18 | 47±19 | 6.5±0.25 | 5.47±1.64 |
| NGC 4536 | 15.6±11.9 | 11±6.7 | 24±10 | 27±11 | 5.8±0.24 | 2.41±0.72 |
| NGC 4605 | 1.8±1 | 1.4±0.8 | 3.0±1.2 | 3.4±1.3 | 0.5±0.03 | 0.11±0.03 |
| NGC 4639 | 14.1±4.7 | 10±6.1 | 19±8.2 | 20±8.4 | 2.2±0.15 | 0.24±0.07 |
| NGC 4725 | 46.2±26.4 | 33±19 | 58±24 | 60±24 | 5.3±0.19 | 0.01±0.00 |
| NGC 5584 | 2.9±4.2 | 7.2±4.2 | 11±4.7 | 12±5.1 | 2.6±0.15 | 0.91±0.27 |
| NGC 7331 | 123.6±70.4 | 53±31 | 107±45 | 118±47 | 12±0.94 | 11±3.31 |
| NGC 7793 | 2.4±1 | 1.5±0.9 | 2.9±1.2 | 3.2±1.3 | 1.4±0.09 | 0.45±0.13 |

Table 2. Stellar and gas masses of the sample galaxies. Column (1): galaxy name; Column (2-5): stellar mass, estimated with different methods: 1– using SED-fitting, 2– using dynamical $\Upsilon_{\star}^{Dyn,K} = 0.29$, 3– using Υ_{\star} as a function of [3.6]-[4.5] colour, 4– using constant $\Upsilon_{\star} = 0.5$; Column (6): total mass of the atomic gas, including contribution of helium and heavier elements; Column (7): total mass of the molecular gas, including contribution of helium and heavier elements; a) we remind that there is no data available for NGC 224 in the K-band. Therefore it lacks a stellar mass estimate based on the second method.

of the individual baryonic components: stellar mass, atomic gas mass and molecular gas mass, as listed in Table 2:

$$M_{bar,m} = M_{\star,m} + M_{atom} + M_{mol}, \quad (15)$$

where $M_{\star,m}$ is one of four stellar masses, estimated with the four different methods ($m = 1, 2, 3, 4$). We further calculate the error on the baryonic mass by applying a full error propagation calculation:

$$\Delta M_{bar,m} = \sqrt{\Delta M_{\star,m}^2 + \Delta M_{atom}^2 + \Delta M_{mol}^2}, \quad (16)$$

The derivation of $\Delta M_{\star,m}$, ΔM_{atom} and ΔM_{mol} is described in Sections 4 & 5.

Consequently, we obtain 12 BTFRs for which we measure slope, scatter and tightness. To be able to perform a fair comparison with the statistical properties of the luminosity-based TFR, we calculate the above mentioned values of scatter and tightness in the BTFRs in the same manner as described in P17. All 12 relations are shown in Figure 9 together with the best fit models of the form $\log M_{bar} = a \times \log V_{rot} + b$.

First, we perform an orthogonal fit to the data points, where the best-fit model minimises the orthogonal distances

from the data points to the model. We use the python implementation of the *BCES* fitting method (Akritas & Bershady 1996; Nemmen et al. 2012), which allows to take correlated errors in both directions into account. Moreover, with this method we assign less weight to outliers and to data points with large error bars. Subsequently, we calculate the vertical scatter σ and the perpendicular tightness σ_{\perp} of each relation as described in P17.

Figure 10 shows the slope, scatter and tightness of the BTFRs for different rotational velocity measures and using different stellar mass estimates. We find that the BTFR with the stellar mass estimated from the SED-fitting ($M_{bar,1}$) shows the largest observed vertical and perpendicular scatter. Next, the BTFR with the stellar mass based on the DMS-motivated dynamical mass-to-light ratio estimate of $\langle \Upsilon_{\star}^{Dyn,K} \rangle = 0.29$ ($M_{bar,2}$), demonstrates somewhat less scatter and appears to be tighter. However, the tightest BTFRs with the smallest vertical scatter are those BTFRs with higher stellar mass-to-light ratios ($M_{bar,3}$ and $M_{bar,4}$). Moreover, all the BTFRs demonstrate a shallower slope and a larger scatter, and are less tight compared to the 3.6 μm luminosity-based TFR (P17). This result is contrary to previous studies (McGaugh et al. 2000; McGaugh 2005), since it suggests that inclusion of the gas mass does not help to

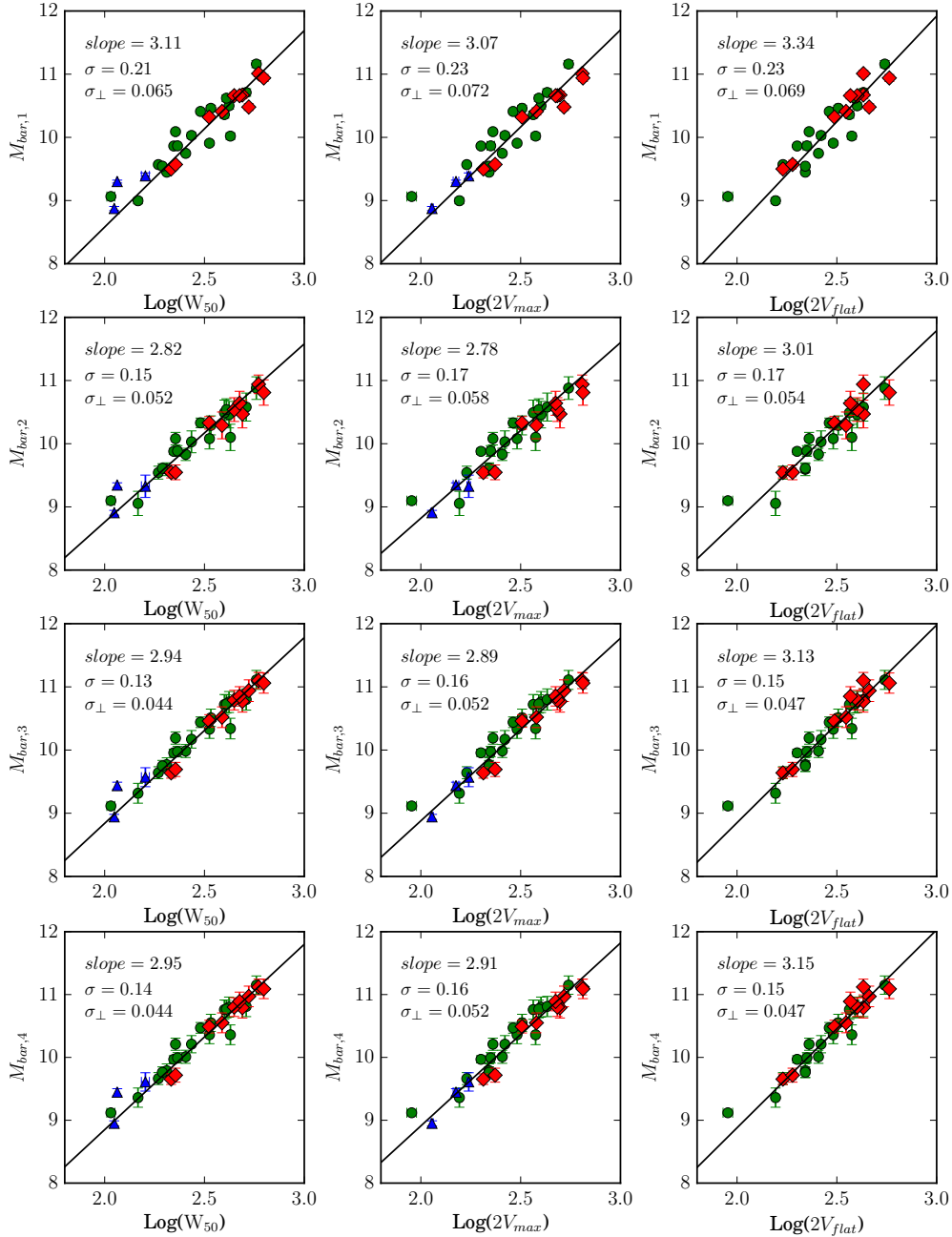


Figure 9. The BTFRs based on the different rotational velocity measures and using different stellar mass estimates. From top to bottom 1. using SED-fitting; 2. using dynamical mass-to-light ratio calibration $\langle \Upsilon_{\star}^{Dyn,K} \rangle = 0.29$; 3. using $\Upsilon_{\star}^{[3.6],cor}$ as a function of $[3.6] - [4.5]$ colour; 4. using constant $\Upsilon_{\star}^{[3.6]} = 0.5$. The best-fit models are shown with solid lines. Green symbols show flat rotation curves ($V_{max} = V_{flat}$), and red symbols indicate galaxies with declining rotation curves ($V_{max} > V_{flat}$). Blue symbols indicate galaxies with rising rotation curves ($V_{max} < V_{flat}$). These galaxies were not included when fitting the model.

tighten the TFR. Instead, it introduces additional scatter, especially for the lower stellar mass-to-light ratios.

We performed a test by assigning different mass-to-light ratios in the $3.6 \mu\text{m}$ band for our sample. We vary mass-to-light ratios from 0.1 to 10, but assign the same value to all galaxies. From Figure 11 it is also clear, that increasing the mass-to-light ratio helps to reduce the vertical scatter and improve the tightness of the BTFR, suggesting that the scatter in the BTFR is introduced by the gaseous

component. From Figure 11 it is also clear that the contribution of the molecular gas component does not significantly affect the statistical properties of the BTFR.

The other important result from our study is that, independent of the stellar mass estimate, each BTFR shows a smaller scatter and improved tightness when based on W_{50} as a rotational velocity measure. This result is also in contradiction with theoretical hypotheses concerning the origin of the TFR, being a relation between the baryonic mass of a

| M_{bar} | Slope | | | Zero point | | |
|-------------|-----------------|-----------------|-----------------|-----------------|-----------------|-----------------|
| | W_{50} | V_{max} | V_{flat} | W_{50} | V_{max} | V_{flat} |
| $M_{bar,1}$ | 3.11 ± 0.19 | 3.07 ± 0.27 | 3.34 ± 0.31 | 2.36 ± 0.48 | 2.49 ± 0.70 | 1.90 ± 0.80 |
| $M_{bar,2}$ | 2.82 ± 0.14 | 2.78 ± 0.20 | 3.01 ± 0.24 | 3.12 ± 0.36 | 3.26 ± 0.53 | 2.76 ± 0.61 |
| $M_{bar,3}$ | 2.94 ± 0.11 | 2.89 ± 0.19 | 3.13 ± 0.21 | 2.96 ± 0.30 | 3.10 ± 0.48 | 2.59 ± 0.54 |
| $M_{bar,4}$ | 2.95 ± 0.11 | 2.91 ± 0.18 | 3.15 ± 0.21 | 2.95 ± 0.29 | 3.09 ± 0.47 | 2.58 ± 0.53 |

Table 3. The statistical properties of the BTFRs. Column (1): Baryonic mass of a galaxy with different stellar mass estimations; Column (2)-Column(4): slopes of the BTFRs based on W_{50} , V_{max} and V_{flat} ; Column (5)-Column(7): zero points of the TFrs based on W_{50} , V_{max} and V_{flat}

| | vertical scatter (σ) | | | tightness (σ_{\perp}) | | |
|-------------|-------------------------------|-----------------|-----------------|--------------------------------|-------------------|-------------------|
| | W_{50} | V_{max} | V_{flat} | W_{50} | V_{max} | V_{flat} |
| $M_{bar,1}$ | 0.21 ± 0.01 | 0.23 ± 0.02 | 0.23 ± 0.02 | 0.065 ± 0.008 | 0.072 ± 0.004 | 0.069 ± 0.004 |
| $M_{bar,2}$ | 0.15 ± 0.01 | 0.17 ± 0.01 | 0.17 ± 0.01 | 0.052 ± 0.006 | 0.058 ± 0.003 | 0.054 ± 0.003 |
| $M_{bar,3}$ | 0.13 ± 0.01 | 0.16 ± 0.01 | 0.15 ± 0.01 | 0.044 ± 0.005 | 0.052 ± 0.002 | 0.047 ± 0.002 |
| $M_{bar,4}$ | 0.14 ± 0.01 | 0.16 ± 0.01 | 0.15 ± 0.01 | 0.044 ± 0.006 | 0.052 ± 0.002 | 0.047 ± 0.002 |

Table 4. The statistical properties of the BTFRs (continued). Column (1): Baryonic mass of a galaxy with different stellar mass estimations; Column (2)-Column(4): scatters of the BTFRs based on W_{50} , V_{max} and V_{flat} ; Column (5)-Column(7): tightnesses of the BTFRs based on W_{50} , V_{max} and V_{flat} .

galaxy and that of its host dark matter halo. Only V_{flat} can properly trace the gravitational potential of a dark matter halo, because it is measured in the outskirts of the extended HI disk where the potential is dominated by the dark matter halo. However, it is also important to note that the scatter and tightness of the BTFR based on W_{50} and on V_{flat} are consistent within their error. Tables 3 & 4 summarise the statistical properties of the BTFRs.

7 OUR ADOPTED BARYONIC TULLY–FISHER RELATION

As was described in the previous sections, the choice of the stellar mass-to-light ratio is not straightforward and requires an evaluation of estimates based on various methods, e.g. from stellar population modelling, or from dynamical modelling. Interestingly, from our SED-fitting and from the dynamical estimate of Υ_{*}^K from the DMS, we obtained the same median of $\langle \Upsilon_{*}^K \rangle \sim 0.3$ (Figure 7) for galaxies that cover similar morphological types. However, the method of estimating the mass-to-light ratio as a function of the [3.6]–[4.5] colour gives a somewhat larger mass-to-light ratios with a much smaller scatter; $\Upsilon_{*}^{[3.6],cor}$ lies in the range between 0.44 and 0.49.

From Section 5.5 we conclude that the individual mass-to-light ratios from the SED-fitting are not applicable to our galaxies, as their values show a large scatter, including unrealistically low mass-to-light ratios for several galaxies. From our study of the statistical properties of the individual BTFRs we also can not draw certain conclusions regarding which stellar mass-to-light ratio to adopt, as the scatter in the BTFR for each case is driven by the gas component (see Section 6). Therefore, for a more detailed study of the BTFR we adopt an intermediate value of the mass-to-light ratio in 3.6 μm band between the high values coming from methods 3 & 4 and the low values coming from methods 1 & 2. Hence, we adopt the final mass-to-light ratio of $\Upsilon_{*}^{fin,[3.6]} = 0.35$, which we assign to all galaxies in our sample.

We calculate the baryonic mass of our sample galaxies

$M_{bar,fin}$, according to Eq. 15 with the stellar mass measured as $M_{*,fin} = \Upsilon_{*}^{fin,[3.6]} \cdot L_{[3.6]}(L_{\odot})$. Figure 12 shows our final BTFR relations based on the three velocity measures W_{50} , V_{max} and V_{flat} . The $M_{bar,fin}$ - V_{flat} , BTFR according to our fit, can be described as

$$M_{bar,fin} = (2.99 \pm 0.22) \cdot \log(2V_{flat}) + 2.88 \pm 0.56. \quad (17)$$

Eq. 17 describes the relation with an observed vertical scatter of $\sigma = 0.16 \pm 0.1$ dex and a tightness of $\sigma_{\perp,obs} = 0.052 \pm 0.013$ dex. These results are consistent with recent studies of the vertical (Lelli et al. 2016) and perpendicular (Papastergis et al. 2016) scatters of the BTFR, but are somewhat larger compared to the 3.6 μm luminosity-based TFR (P17). Importantly, our slope and scatter are consistent with the mean value for these parameters as a function of BTFR sample size (Sorce & Guo 2016). The contributions from the stellar and gaseous components to the BTFR separately are shown in Figure 13

Furthermore, we investigate the intrinsic tightness of the BTFR. We are focusing on the tightness and not on the vertical scatter of the relation, because the tightness is a slope independent measure and should be used as a possible constraint on theories of galaxy formation and evolution. We compare the perpendicular distances $d_{\perp,i}$ of the data points to the line, with the projected measurement errors ϵ_i based on the error on the baryonic mass ($\Delta M_{bar,i}$) and the error on the rotational velocity ($\epsilon_{V_{flat,i}}$) (see P17 for more details). Figure 14 shows the histogram of $d_{\perp,i}/\epsilon_i$. In the case of zero intrinsic scatter σ_{\perp} , this histogram would follow the standard normal distribution, shown with the dashed Gaussian curve in Figure 14. However, it is clear that the distribution of $d_{\perp,i}/\epsilon_i$, shown with the solid Gaussian curve, is broader with a standard deviation of 1.33 ± 0.2 . Consequently, we can estimate the value of the intrinsic $\sigma_{\perp,int}$ as follows:

$$\sigma_{\perp,int} = \sqrt{\sigma_{\perp,obs}^2 - \sigma_{\perp,err}^2}, \quad (18)$$

where $\sigma_{\perp,err} = 0.045$ dex is the perpendicular scatter due to the measurement uncertainties only. Hence, we estimate the

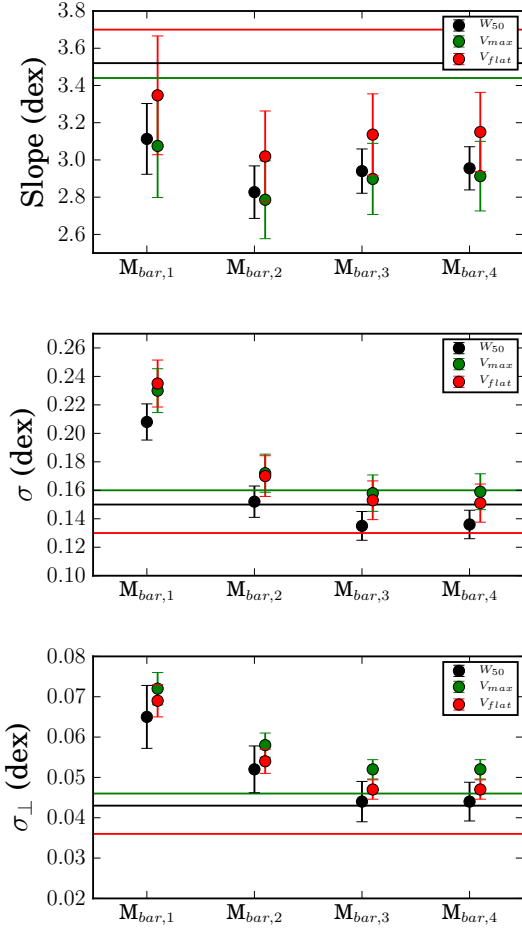


Figure 10. The slope, vertical scatter and tightness of the BT-Frs. Black symbols indicate the values for the relation based on W_{50} as a rotational velocity measure, green on V_{max} and red on V_{flat} . The values are presented for the BT-Frs, using different stellar mass estimates: 1. SED-fitting; 2. dynamical $\langle \Upsilon_{\star}^{Dyn,K} \rangle = 0.29$; 3. $\Upsilon_{\star}^{[3.6],cor}$ as a function of $[3.6] - [4.5]$ colour; 4. constant $\Upsilon_{\star}^{[3.6]} = 0.5$. The solid lines show the slope, scatter and tightness of the $3.6 \mu\text{m}$ luminosity-based TFr based on the different rotational velocity measures.

$\sigma_{\perp, int} \sim 0.026 \pm 0.013$ dex, which is identical to the $\sigma_{\perp, int}$ of the $3.6 \mu\text{m}$ luminosity-based TFr (P17). Therefore, we can conclude that even if the BT-Fr has a larger observed perpendicular scatter compared to the $3.6 \mu\text{m}$ luminosity-based TFr, it is only due to the measurement uncertainties because both relations have the same intrinsic perpendicular scatter $\sigma_{\perp, int} \sim 0.026$ dex.

7.1 Search for a 2nd parameter

As was suggested by various authors (Aaronson & Mould 1983; Rubin et al. 1985), the vertical scatter in the luminosity-based TFr at optical wavelengths can be decreased by invoking a second parameter. However, we demonstrated in P17 that the residuals of the $3.6 \mu\text{m}$ TFr do not correlate significantly with any of the galactic properties and, therefore, we could not identify any second parameter that could further reduce the scatter. Verheijen (2001)

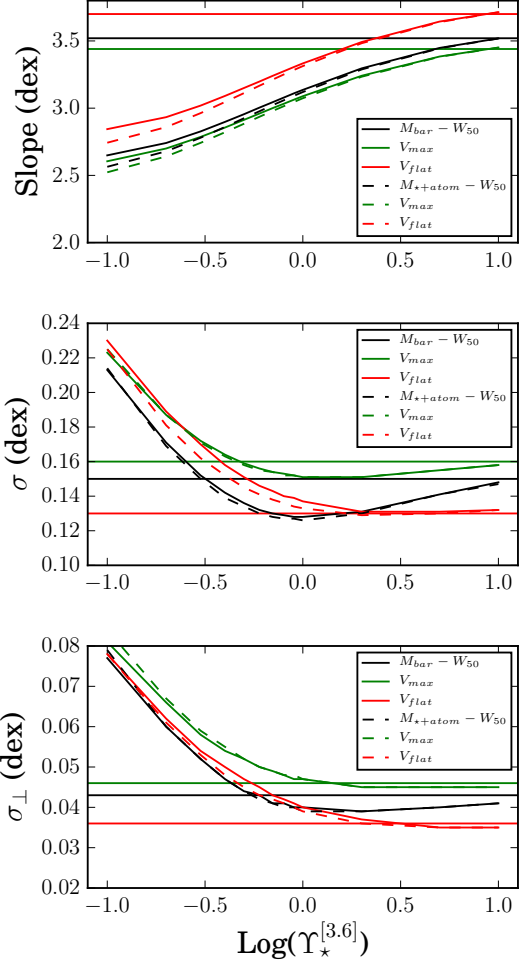


Figure 11. The slope, vertical scatter and tightness of the BT-Frs as a function of the mass-to-light ratio in the $3.6 \mu\text{m}$ band. Black lines indicate the values for the relation based on W_{50} as a rotational velocity measure, green on V_{max} and red on V_{flat} . The solid lines show the trends for the BT-Fr ($M_{\star} + M_{atom} + M_{mol}$). The dashed lines show the trends for $M_{\star} + M_{atom}$. The solid horizontal lines show the slope, scatter and tightness of the $3.6 \mu\text{m}$ luminosity-based TFr based on the different rotational velocity measures.

reached the same conclusion for the K-band $M_K - V_{flat}$ TFr constructed with Ursa Major galaxies. In this section we repeat this exercise for the $M_{bar, fin} - V_{flat}$ relation and examine the nature of the residuals along the fitted model line described by Eq. 17. Figure 15 presents the residuals of the BT-Fr ($\log \Delta M_{bar}$) as a function of global galactic properties, such as star formation rate, outer slope of the rotation curve, central surface brightness, $i - [3.6]$ colour, and gas fraction. We calculate ΔM_{bar} as $\Delta M_{bar} = M_{bar} / M_{bar, model}$, where $M_{bar, model}$ is described by Eq. 17.

To quantitatively describe the strength of the correlations we calculate Pearson's correlation coefficients r for each of the relations. We find the largest $r = 0.48$ for the correlation between ΔM_{bar} and the total gas fraction ($f_{gas} = (M_{atom} + M_{mol}) / M_{bar}$) and the smallest $r = 0.02$ for the correlation between ΔM_{bar} and $i - [3.6]$ colour. Even though the strength of neither correlations is sufficient to

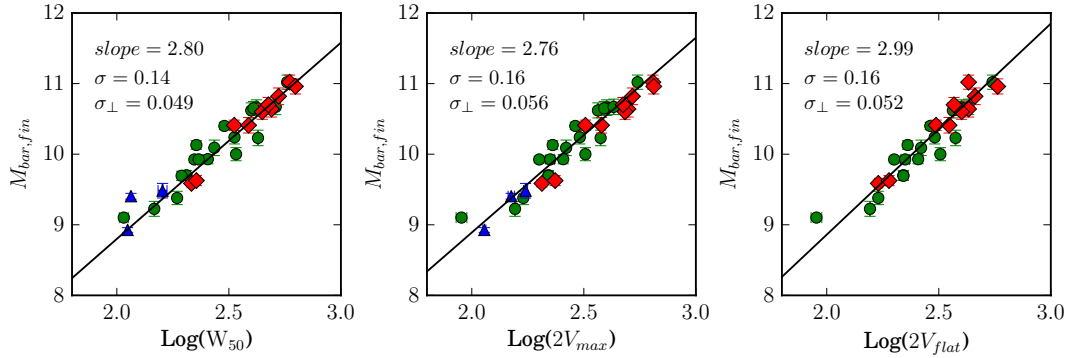


Figure 12. The final BTFR based on the three velocity measures (W_{50} , V_{max} and V_{flat}) with the baryonic mass calculated as $M_{bar,fin} = M_{*,fin} + M_{atom} + M_{mol}$. The best-fit models are shown with solid lines. Green symbols show galaxies with flat rotation curves ($V_{max} = V_{flat}$), and red symbols indicate galaxies with declining rotation curves ($V_{max} > V_{flat}$). Blue symbols indicate galaxies with rising rotation curves ($V_{max} < V_{flat}$). These galaxies were not included when fitting the model.

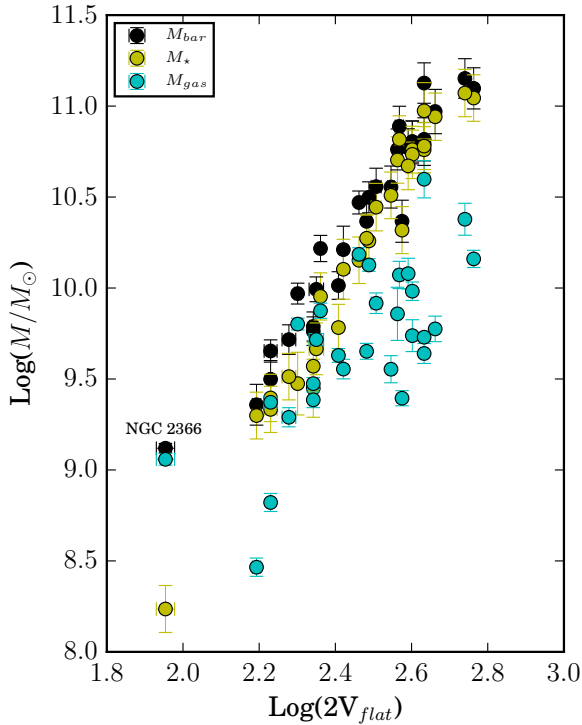


Figure 13. The final choice BTFR based on V_{flat} is shown with the black symbols. The stellar component is shown with the yellow symbols and the gaseous component with the cyan symbols.

identify a significant second parameter, a possible correlation between ΔM_{bar} and f_{gas} could explain why studies based on gas-rich galaxies (McGaugh 2012; Papastergis et al. 2016) find generally steeper slopes.

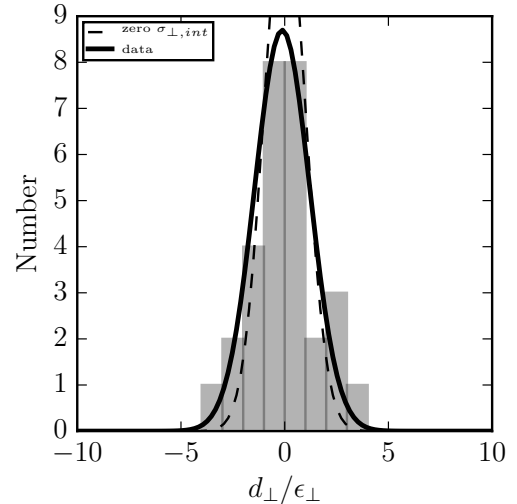


Figure 14. Histogram of the perpendicular distances from the data points to the line (d_{\perp}) in $M_{bar,fin}-V_{flat}$ relation, normalised by the perpendicular errors. The standard normal distribution that would be expected for a zero intrinsic tightness is shown with dashed line. The best-fit to the data, weighted by the Poisson errors, is shown with the solid line with a standard deviation of 1.33 ± 0.2 .

8 COMPARISON WITH PREVIOUS OBSERVATIONAL STUDIES AND THEORETICAL RESULTS

8.1 Previous studies

The biggest challenge in comparing our measurements of the statistical properties of the BTFR with other studies is posed by the different methods used to derive the main galaxy properties such as their baryonic mass and rotational velocity (Bradford et al. 2016). For instance, the galaxy sample, the mass range of galaxies, the applied corrections and the choice of the fitting method contribute significantly to the measurement uncertainties. Moreover, it is critical in the comparison that the rotational velocities are similarly defined. Therefore, it is important to note that we consider

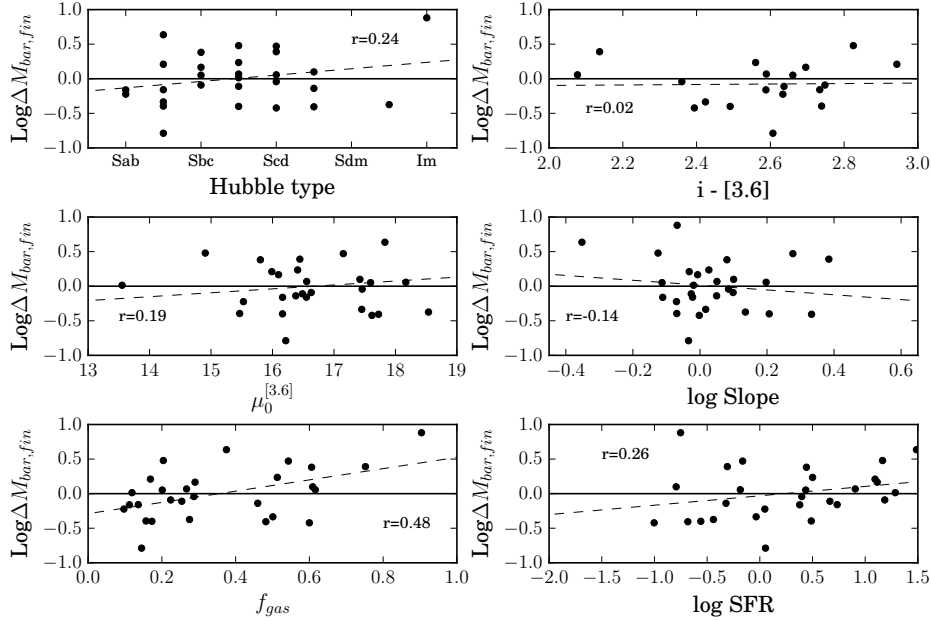


Figure 15. Residuals of the $M_{bar,fin} - 2V_{flat}$ relation as a function of global galactic properties. r is Pearson's correlation coefficient.

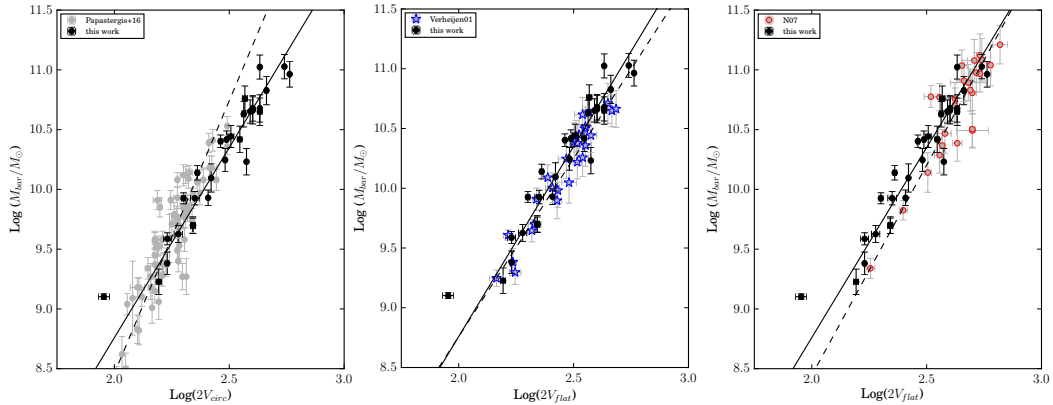


Figure 16. The comparison between our BTFr sample and previous studies: left panel from Papastergis et al. (2016); middle panel from Verheijen (2001) and right panel from Noordermeer & Verheijen (2007). With solid lines the fits for our sample are shown and with dashed lines the fits for previous studies are shown.

our $M_{bar,fin} - 2V_{flat}$ relation for these comparisons. However, it is not always the case that previous studies of the BTFr are based on $2V_{flat}$ as a rotational velocity measure. In the literature, it is more common that the global HI profile widths are used to estimate the circular velocity and, therefore, we further refer to the rotational velocity in general as V_{circ} .

Our results are in a good agreement with those by Lelli et al. (2016) and McGaugh (2012) who both use $V_{circ} = V_{flat}$. We obtain the observed vertical scatter $\sigma = 0.16$ dex to be similar with the one reported by Lelli et al. (2016) and our observed tightness $\sigma_{\perp} = 0.052$ dex is consistent with the total tightness $\sigma_{\perp} = 0.06$ dex found by McGaugh (2012). However, we find a shallower slope than the above mentioned studies. The slope of the BTFr reported by both Lelli et al. (2016) and McGaugh (2012) is measured to be

$a \approx 4$, while we find the slope of the BTFr to be $a \approx 3$. This can be understood as they applied a higher stellar mass-to-light ratio ($\Upsilon_{*}^{3.6} = 0.5$ for the disk) which reduces the relative contribution of the gas to M_{bar} such that their BTFr approaches our $L_{[3.6]} - 2V_{flat}$ relation. They also do not include the presence of the molecular gas in intermediate- and high-mass spirals in their study. Our slope is more consistent with the result by Zaritsky et al. (2014), who find the slope of the BTFr to be in the range from $a = 3.3$ to $a = 3.5$, however they used the corrected width of the global HI profile $V_{circ} = W_{50}^2/2$.

The low mass end of the BTFr is not well populated by our sample. Moreover, the low-mass galaxies tend to have rotation curves that are still rising at their outermost measured point and, therefore, can not be considered for the $M_{bar,fin} - 2V_{flat}$ relation. Furthermore, the only low-mass

| | This work | Verheijen01 | Noordermeer+07 | Papastergis+16 |
|------------------|-----------|-------------|----------------|----------------|
| slope | 2.99 | 2.98 | 3.51 | 4.58 |
| zero point | 2.88 | 2.82 | 1.4 | -0.66 |
| σ | 0.16 | 0.12 | 0.20 | 0.23 |
| σ_{\perp} | 0.052 | 0.045 | 0.058 | 0.053 |

Table 5. Slope, zero point, scatter and tightness of the BTFRs from different studies Column(1): name of the parameter; Column (2): slope, zero point, scatter and tightness from this work; Column (3): slope, zero point, scatter and tightness from Verheijen (2001); Column (4): slope, zero point, scatter and tightness from Noordermeer & Verheijen (2007); Column (5): slope, zero point, scatter and tightness from Papastergis et al. (2016).

galaxy in our sample (NGC 2366) appears to be very gas rich (see Figure 13). If we remove this galaxy from the fit, the statistical properties of our BTFR change slightly, as the observed tightness changes from $\sigma_{\perp} = 0.052$ to $\sigma_{\perp} = 0.048$ dex. However, there is nothing unusual about NGC 2366 that would allow us to remove it from the BTFR. Moreover, it clearly demonstrates that inclusion of the gaseous component in the TFR increases its scatter, as NGC 2366 is not an outlier on the luminosity-based TFR of our sample.

For a more detailed comparison with previous studies, we present the comparison analysis of the statistical properties of our BTFRs with the BTFR from Papastergis et al. (2016); Verheijen (2001) and Noordermeer & Verheijen (2007). The sample from Papastergis et al. (2016) is a sample of heavily gas-dominated ($M_{gas}/M_{\star} \geq 2.7$) galaxies that populate the low-mass end of the BTFR (M_{\star} in a range from 3×10^8 to $3 \times 10^{10} M_{\odot}$), where V_{circ} was measured as $V_{circ} = W_{50}^i/2$. From this sample we adopt only those 68 galaxies that have a large negative kurtosis ($h4 < -1.2$) of their global HI profile, indicating that this profile is double-peaked. Therefore, in these galaxies $W_{50}^i/2$ is most likely a good approximation of V_{flat} . The sample from Verheijen (2001) is the Ursa Major sample of intermediate mass galaxies (M_{\star} in the range from 1.6×10^9 to $4.0 \times 10^{10} M_{\odot}$) where $V_{circ} = V_{flat}$ was measured in the same manner as in our study, and $M_{\star} = 0.4L_{\star, K_s}$. The Noordermeer & Verheijen (2007) sample is a sample of higher mass galaxies (M_{\star} in the range from 2.0×10^9 to $2.0 \times 10^{11} M_{\odot}$) where $V_{circ} = V_{flat}$ and $M_{\star} = 0.4L_{\star, K_s}$ as well. It is critical for the comparison of the BTFR studies that the fitting algorithm is defined similarly (Bradford et al. 2016). Therefore, we apply our fitting routine to the above-mentioned samples from Papastergis et al. (2016); Verheijen (2001) and Noordermeer & Verheijen (2007), in order to derive the statistical properties of the BTFRs in the same way as we did in our study. In Figure 16 we present the comparisons between our sample and those three from the literature. The low-mass end and the high-mass end samples show different results in comparison to our BTFR. For instance, the slope of the high-mass end sample (Noordermeer & Verheijen 2007) is equal to $a = 3.51$, while the slope of the low-mass sample (Papastergis et al. 2016) has the value of $a = 4.58$. Meanwhile, the statistical properties of the Verheijen (2001) Ursa Major BTFR and our BTFR are in excellent agreement, as the data for both these samples have been treated in the same way (see Figure 16 and Table 5).

The other important issue to keep in mind is that the baryonic masses of galaxies were measured in different ways in the various studies. This may also contribute to the differences we find while performing these comparisons. For example, Papastergis et al. (2016) use the average value of

the stellar mass as derived with five different methods for each galaxy in the sample¹ and $M_{gas} = 1.3 \times M_{HI}$. Zaritsky et al. (2014) adopt a stellar mass as measured from the ratio of the 3.6 and 4.5 μm fluxes. Lelli et al. (2016) and McGaugh (2012) adopt a single mass-to-light ratio for all galaxies equal to $\Upsilon_{\star}^{3.6} = 0.5$ for the disk. The results for our BTFR with the adopted stellar mass-to-light ratio equal to $\Upsilon_{\star}^{3.6} = 0.5$ are presented in Section 6, and we recall that this choice of $\Upsilon_{\star}^{3.6} = 0.5$ for our sample also results in a shallower slope of $a = 3.15 \pm 0.21$ for the BTFR.

8.2 Semi-analytical models

In the DM-only simulations within the Λ CDM cosmological model framework the mass of the DM halo relates to its rotational velocity as $M_h \propto V_{h,max}^3$. Therefore, the BTFR just follows from this relation as $M_{bar} \propto V_{rot}^3$ (Klypin et al. 2011). A further study of the BTFR in the Λ CDM context is done by using semi-analytical models (SAMs) of galaxy formation which assign observationally motivated masses of stars and gas to the host dark matter halo, and V_{circ} is usually calculated by computing the rotation curve, which takes into account the contribution of the baryons to the total gravitational potential from which the rotation curve is calculated (Moster et al. 2010; Trujillo-Gomez et al. 2011). Consequently, the value of V_{circ} is either determined at a particular radius or is assumed to be the rotational velocity of the peak of the simulated rotation curve $V_{circ} = V_{max}$.

We compare our BTFR with those from two SAMs from Trujillo-Gomez et al. (2011) and from Desmond (2012). From Trujillo-Gomez et al. (2011) we consider two models: one in which DM halos experience adiabatic contraction due to the infall of the baryons to the halo centres, and one without adiabatic contraction. The rotation velocity in Trujillo-Gomez et al. (2011) is calculated at a fixed radius of 10 kpc. The semi-analytical model of Desmond (2012) uses the $V_{circ} = V_{max}$ estimation of the rotational velocity. Moreover, the Desmond (2012) model also calculates the intrinsic scatter of the BTFR, expected in a Λ CDM cosmology. This scatter is caused by various mechanisms, such as scatter in the concentration parameter of the DM halos, scatter in the halo spin parameter and scatter in the baryon fraction of the halo. Figure 17 presents the comparison of our sample BTFR (left panel) and of the combined sample with those from Verheijen (2001) and Noordermeer & Verheijen (2007) (right panel) with these two models. Note that for the

¹ 1. using SED-fitting of the SDSS bands; 2. using SED-fitting of the SDSS + GALEX bands; 3. using $g - i$ colour; 4. using constant $\Upsilon_{\star} = 0.45$ in 3.4 μm band; 5. using constant $\Upsilon_{\star} = 0.6$ in K-band.

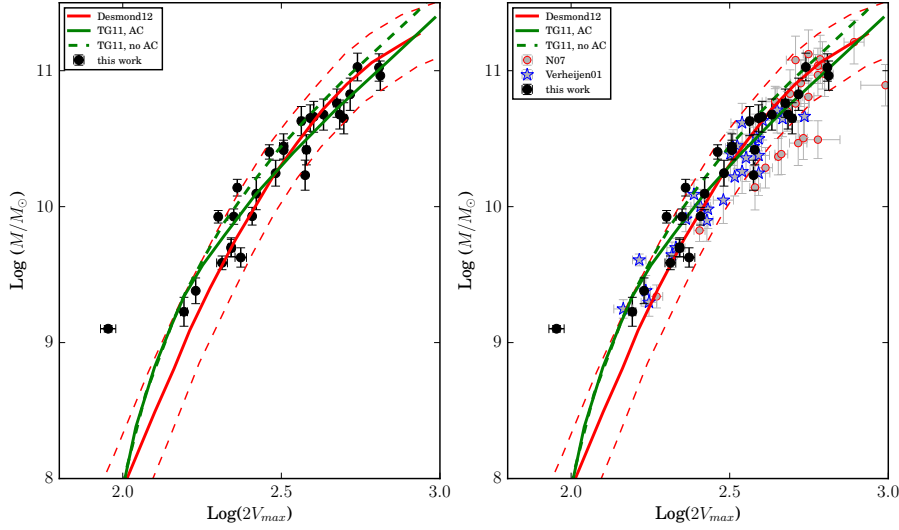


Figure 17. Left panel: The comparison between our BTFR with the SAMs from [Trujillo-Gomez et al. \(2011\)](#) (with adiabatic contraction (solid green line) and without (dashed green line)) and with the semi-analytic model from [Desmond \(2012\)](#) (red line). With dashed red lines the 2σ intrinsic scatter is indicated. Right panel: the same comparisons but of the combined sample with [Noordermeer & Verheijen \(2007\)](#) (red circles) and [Verheijen \(2001\)](#) (blue stars).

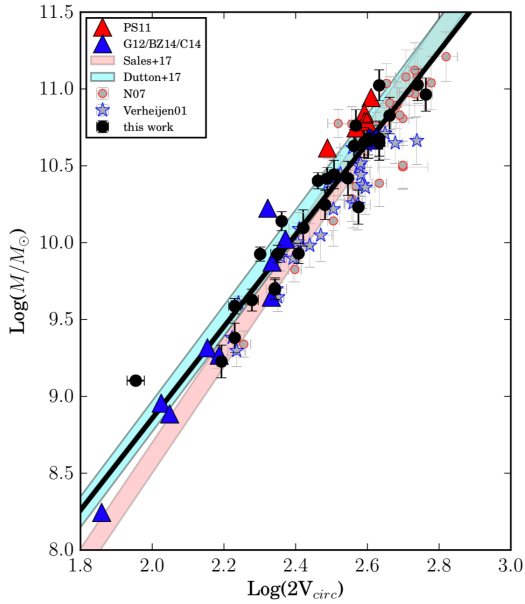


Figure 18. The comparison of our BTFR combined with [Noordermeer & Verheijen \(2007\)](#) (red circles) and [Verheijen \(2001\)](#) (blue stars) samples, with the galaxies produced by the hydrodynamical simulations from [Piontek & Steinmetz \(2011\)](#) (red triangles), and by [Governato et al. \(2012\)](#); [Brooks & Zolotov \(2014\)](#) and [Christensen et al. \(2014\)](#) (blue triangles). The best-fit BTFR with the measured scatter from the APOSTLE/EAGLE simulations is shown with red shaded area ([Sales et al. 2017](#)). The NIHAO simulations best-fit BTFR with the measured scatter is shown with the cyan area ([Dutton et al. 2017](#)).

observational samples we use $V_{circ} = V_{max}$ for a fair comparison. The slight curvature in the BTFR that is present in both models is a general prediction of SAMs in the Λ CDM

cosmological model. Both models can reproduce our sample relatively well (Figure 17) with the one clear outlier NGC 2366. Even though the [Desmond \(2012\)](#) model is systematically offset from the observed data points of all three samples, it can reproduce the relations within the 2σ uncertainty accounting for the intrinsic scatter of the BTFR, as indicated with the dashed red lines in Figure 17. It is important to note that, even though SAMs can reproduce our BTFR with 2σ uncertainty, we do not find the presence of curvature in our observed BTFR.

8.3 Hydrodynamical simulations

In Figure 18 we compare our BTFR with individual galaxies produced by hydrodynamical simulations in the context of a Λ CDM cosmological model and with the best-fit BTFR with the measured scatter from the APOSTLE/EAGLE (red shade, [Sales et al. 2017](#)) and the NIHAO (cyan shade, [Dutton et al. 2017](#)) hydrodynamical simulations. While both sets of the simulations are successful in reproducing the high-mass end of our BTFR, the NIHAO works better on the smaller scales. From individual galaxies for the high-mass end of the BTFR we consider eight galaxies from [Piontek & Steinmetz \(2011\)](#) and for the intermediate and low-mass end we consider twelve galaxies, produced in a set of hydrodynamical simulations by [Governato et al. \(2012\)](#); [Brooks & Zolotov \(2014\)](#) and [Christensen et al. \(2014\)](#). In Figure 18 it is shown that these sets of hydrodynamical simulations are successful at reproducing the observed BTFR with the exception of the [Piontek & Steinmetz \(2011\)](#) sample of high mass galaxies, which lies systematically above the observed BTFR. The rotational velocities of galaxies in these simulations are measured from the width of the global HI profiles and therefore, for z fair comparison, we also use W_{50} as a rotational velocity measure for the observational samples.

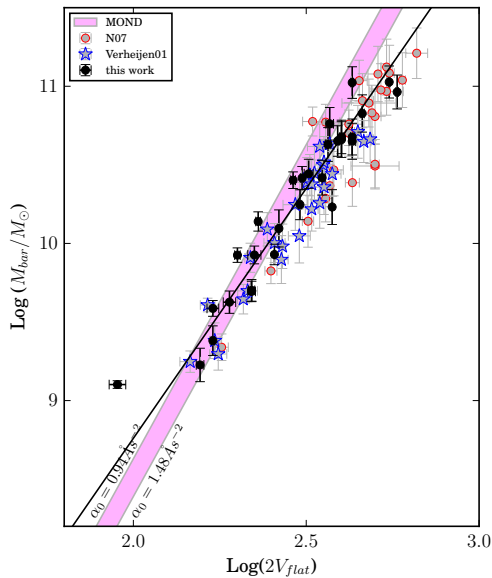


Figure 19. Our BTFR combined with the samples from [Noordermeer & Verheijen \(2007\)](#) and [Verheijen \(2001\)](#) and in comparison with the BTFR predicted by MOND.

8.4 MOND

Modified newtonian dynamics (MOND) is an alternative to the Λ CDM model of galaxy formation and evolution, which does not require the presence of dark matter, but where gravitational forces are entirely defined by the amount and distribution of the baryonic matter ([Milgrom & Braun 1988](#)). Therefore, it predicts that the BTFR with $V_{circ} = V_{flat}$ can be described with a single power-law with zero intrinsic scatter, and the relation has a slope of exactly 4 when it is based on V_{flat} as a rotational velocity measure, while the normalisation of the relation depends only on the acceleration parameter α_0 ([McGaugh 2012](#)).

The advantage of our sample is that it is based on V_{flat} as a rotational velocity measure and therefore allows us to directly compare our results with the predictions from MOND. While the slope and zero intrinsic scatter of the BTFR from the MOND prediction are fixed, the normalisation of the relation can vary due to the uncertainty in the observational determination of the acceleration parameter α_0 ([Begeman et al. 1991](#)). In Figure 19 we consider two values for the acceleration parameter $\alpha_0 = 0.94 \text{ \AA s}^{-2}$ and $\alpha_0 = 1.48 \text{ \AA s}^{-2}$ which are consistent with [Begeman et al. \(1991\)](#). Since we deal mainly with bright galaxies, where the effect of MOND is less obvious than for the dwarfs, we should note that we do not probe deeply into the MOND regime at the faint end of the BTFR. However, from Figure 19 it is clear that, while the MOND normalisation works well for the intermediate mass galaxies, it fails to reproduce the high-mass end of the BTFR (represented by our, [Verheijen \(2001\)](#) and [Noordermeer & Verheijen \(2007\)](#) samples) by introducing a slope that is too steep. In conclusion, neither the non-zero intrinsic scatter nor the slope of our BTFR are consistent with the relation predicted by MOND.

9 SUMMARY AND CONCLUSIONS

In this paper we perform a detailed study of the Baryonic Tully–Fisher relation based on different stellar mass estimates and taking advantage of a sample with accurate primary distance measurements, homogeneously analysed photometry, and spatially resolved HI kinematics. The aim of our study is to investigate how the various stellar mass estimation methods affect the statistical properties of the BTFR. For this, we estimate the stellar masses of our sample galaxies following four different prescriptions. First, we measured stellar masses by performing a full SED-fitting using 18 photometric bands (from FUV to far infrared). Second, we adopt a median value of the dynamical mass-to-light ratio from the DiskMass survey $\Upsilon_{*}^{Dyn,K} = 0.3$. Then, we calculate the stellar mass-to-light ratio for the $3.6 \mu\text{m}$ band as a function of $[3.6]-[4.5]$ colour and, finally, we adopt the single mass-to-light ratio equal to $\Upsilon_{*}^{[3.6]} = 0.5$ from [Lelli et al. \(2016\)](#), which is motivated by an empirical minimisation of the vertical scatter in the BTFR.

Using each stellar mass estimate, we construct the Baryonic Tully–Fisher relations. Each of the relations is based on three different velocity measures: W_{50} from the global HI profile, and V_{max} and V_{flat} from the rotation curve. For each of the relations we measure the slope, vertical scatter and tightness. We find that the tightest BTFRs with the smallest vertical scatter are those based on larger mass-to-light ratios (method 3 and method 4) and based on W_{50} as a rotational velocity measure. However, none of the relations demonstrates as small a vertical and perpendicular scatter as the $3.6 \mu\text{m}$ luminosity-based TFR. This allows us to conclude that mostly the gas component is responsible for the increase of the scatter (vertical and perpendicular) in the BTFR. Hence, increasing the mass-to-light ratio reduces the vertical and perpendicular scatter of the BTFR, as it makes the gas contribution negligible.

We consider in detail our BTFR of choice, which is based on V_{flat} and a stellar mass computed with a single mass-to-light ratio $\Upsilon_{*}^{[3.6]} = 0.35$. This choice of the mass-to-light ratio is motivated by adopting a value intermediate between the high values of methods 3 and 4 and low values of methods 1 and 2. We measure the slope, vertical scatter and tightness of our BTFR. We find the slope equal to 2.99 ± 0.28 , which is shallower in comparison with previous studies ([Lelli et al. 2016](#); [McGaugh 2012](#)), and the vertical scatter $\sigma = 0.16$ dex, which is consistent with the previous study by [Lelli et al. \(2016\)](#). We find the observed tightness $\sigma_{\perp} = 0.052$ dex to be smaller than the ones found by [Papaastergier et al. \(2016\)](#) and [McGaugh \(2012\)](#). This observed perpendicular scatter is larger than the perpendicular scatter of the $3.6 \mu\text{m}$ luminosity-based TFR (P17). However, the estimated intrinsic perpendicular scatter is shown to be similar $\sigma_{\perp,int} \sim 0.026 \pm 0.13$ dex.

Furthermore, we compare the results of our BTFR with various theoretical predictions from Λ CDM theories of galaxy formation and MOND. We find that semi-analytic models ([Trujillo-Gomez et al. 2011](#); [Desmond 2012](#)) and different sets of cosmological hydrodynamical simulations ([Dutton et al. 2017](#); [Sales et al. 2017](#)) represent our relation reasonably well within the allowed 2σ uncertainty. Moreover, individual galaxies of different masses from various hydrodynamical simulations ([Governato et al. 2012](#); [Brooks](#)

& Zolotov 2014; Christensen et al. 2014; Piontek & Steinmetz 2011) also tend to follow our observed BTFR. However, the predictions from MOND fail to reproduce the observed BTFR at the high-mass end, where the observed galaxies of high masses tend to lie below the MOND predicted relation since the slope predicted by MOND is steeper. Our observed BTFR is shown not to be consistent with a zero intrinsic scatter at the 2σ level.

In conclusion, it is important to point out that there is no unique method to estimate the stellar masses of spiral galaxies. Various methods lead to estimates which may differ significantly from each other. Therefore, the statistical properties of the Baryonic Tully-Fisher relation remain uncertain as different stellar mass-to-light ratios lead to different estimates of the slope, scatter and tightness of the relation.

ACKNOWLEDGEMENTS

AP is grateful to Jayaram Chengalur, Filippo Fraternali and Federico Lelli for useful comments and suggestions. AB acknowledges financial support from the CNES (Centre National d'Etudes Spatiales – France). EP is supported by a NOVA postdoctoral fellowship of the Netherlands Research School for Astronomy (NOVA). MV acknowledges the Netherlands Foundation for Scientific Research support through VICI grant 016.130.338. We acknowledge the Leids Kerkhoven-Bosscha Fonds (LKBF) for travel support. We acknowledge financial support from the DAGAL network from the People Programme (Marie Curie Actions) of the European Union's Seventh Framework Programme FP7/2007-2013/ under REA grant agreement number PITNGA-2011-289313. We thank Elisabete da Cunha for making the MAGPHYS SED-fitting code publicly available.

REFERENCES

Aaronson M., Mould J., 1983, *ApJ*, **265**, 1
 Akritas M. G., Bershady M. A., 1996, *ApJ*, **470**, 706
 Aniyani S., Freeman K. C., Gerhard O. E., Arnaboldi M., Flynn C., 2016, *MNRAS*, **456**, 1484
 Bahcall J. N., Casertano S., 1984, *ApJ*, **284**, L35
 Begeman K. G., Broeils A. H., Sanders R. H., 1991, *MNRAS*, **249**, 523
 Bell E. F., de Jong R. S., 2001, *ApJ*, **550**, 212
 Bendo G. J., et al., 2007, *MNRAS*, **380**, 1313
 Bershady M. A., Verheijen M. A. W., Swaters R. A., Andersen D. R., Westfall K. B., Martinsson T., 2010, *ApJ*, **716**, 198
 Bland-Hawthorn J., Gerhard O., 2016, *ARA&A*, **54**, 529
 Bolatto A. D., Leroy A. K., Rosolowsky E., Walter F., Blitz L., 2008, *ApJ*, **686**, 948
 Bradford J. D., Geha M. C., van den Bosch F. C., 2016, *ApJ*, **832**, 11
 Brook C. B., Santos-Santos I., Stinson G., 2016, *MNRAS*, **459**, 638
 Brooks A. M., Zolotov A., 2014, *ApJ*, **786**, 87
 Bruzual G., Charlot S., 2003, *MNRAS*, **344**, 1000
 Chabrier G., 2003, *ApJ*, **586**, L133
 Charlot S., Fall S. M., 2000, *ApJ*, **539**, 718
 Christensen C. R., Governato F., Quinn T., Brooks A. M., Shen S., McCleary J., Fisher D. B., Wadsley J., 2014, *MNRAS*, **440**, 2843

Conroy C., Gunn J. E., White M., 2009, *ApJ*, **699**, 486
 Courteau S., Rix H.-W., 1999, *ApJ*, **513**, 561
 Dame T. M., Hartmann D., Thaddeus P., 2001, *ApJ*, **547**, 792
 Desmond H., 2012, preprint, ([arXiv:1204.1497](https://arxiv.org/abs/1204.1497))
 Dutton A. A., 2012, *MNRAS*, **424**, 3123
 Dutton A. A., et al., 2017, *MNRAS*, **467**, 4937
 Eskew M., Zaritsky D., Meidt S., 2012, *AJ*, **143**, 139
 Freedman W. L., et al., 2001, *ApJ*, **553**, 47
 Freeman K. C., 1999, in Davies J. I., Impey C., Phillips S., eds, *Astronomical Society of the Pacific Conference Series Vol. 170, The Low Surface Brightness Universe*. p. 3
 Governato F., et al., 2012, *MNRAS*, **422**, 1231
 Harris J., Zaritsky D., 2009, *AJ*, **138**, 1243
 Karachentsev I. D., Kaisina E. I., Kashibadze (Nasonova O. G.), 2017, *AJ*, **153**, 6
 Klypin A. A., Trujillo-Gomez S., Primack J., 2011, *ApJ*, **740**, 102
 Kregel M., van der Kruit P. C., de Grijs R., 2002, *MNRAS*, **334**, 646
 Lelli F., McGaugh S. S., Schombert J. M., 2016, *ApJ*, **816**, L14
 Leroy A. K., et al., 2009, *AJ*, **137**, 4670
 Macciò A. V., Udrescu S. M., Dutton A. A., Obreja A., Wang L., Stinson G. R., Kang X., 2016, *MNRAS*, **463**, L69
 Maraston C., Daddi E., Renzini A., Cimatti A., Dickinson M., Papovich C., Pasquali A., Pirzkal N., 2006, *ApJ*, **652**, 85
 Marigo P., Girardi L., 2007, *A&A*, **469**, 239
 Martinsson T. P. K., Verheijen M. A. W., Westfall K. B., Bershady M. A., Andersen D. R., Swaters R. A., 2013, *A&A*, **557**, A131
 McGaugh S. S., 2005, *ApJ*, **632**, 859
 McGaugh S. S., 2012, *AJ*, **143**, 40
 McGaugh S. S., de Blok W. J. G., 1998, *ApJ*, **499**, 41
 McGaugh S. S., Schombert J. M., Bothun G. D., de Blok W. J. G., 2000, *ApJ*, **533**, L99
 McGaugh S. S., Lelli F., Schombert J. M., 2016, *Physical Review Letters*, **117**, 201101
 Meidt S. E., et al., 2012, *ApJ*, **744**, 17
 Meidt S. E., et al., 2014, *ApJ*, **788**, 144
 Milgrom M., 1983, *ApJ*, **270**, 384
 Milgrom M., Braun E., 1988, *ApJ*, **334**, 130
 Moster B. P., Somerville R. S., Maulbetsch C., van den Bosch F. C., Macciò A. V., Naab T., Oser L., 2010, *ApJ*, **710**, 903
 Navarro J. F., Steinmetz M., 2000, *ApJ*, **538**, 477
 Nemmen R. S., Georganopoulos M., Guiric S., Meyer E. T., Gehrels N., Sambruna R. M., 2012, *Science*, **338**, 1445
 Noordermeer E., Verheijen M. A. W., 2007, *MNRAS*, **381**, 1463
 Norris M. A., Meidt S., Van de Ven G., Schinnerer E., Groves B., Querejeta M., 2014, *ApJ*, **797**, 55
 Paladino R., Murgia M., Helfer T. T., Wong T., Ekers R., Blitz L., Gregorini L., Moscadelli L., 2006, *A&A*, **456**, 847
 Papastergis E., Adams E. A. K., van der Hulst J. M., 2016, *A&A*, **593**, A39
 Peters S. P. C., van der Kruit P. C., Allen R. J., Freeman K. C., 2017, *MNRAS*, **464**, 2
 Pforr J., Maraston C., Tonini C., 2012, *MNRAS*, **422**, 3285
 Piontek F., Steinmetz M., 2011, *MNRAS*, **410**, 2625
 Ponomareva A. A., Verheijen M. A. W., Bosma A., 2016, *MNRAS*, **463**, 4052
 Ponomareva A. A., Verheijen M. A. W., Peletier R. F., Bosma A., 2017, *MNRAS*, **469**, 2387
 Querejeta M., et al., 2015, *ApJS*, **219**, 5
 Rizzi L., Tully R. B., Makarov D., Makarova L., Dolphin A. E., Sakai S., Shaya E. J., 2007, *ApJ*, **661**, 815
 Röck B., Vazdekis A., Peletier R. F., Knapen J. H., Falcón-Barroso J., 2015, *MNRAS*, **449**, 2853
 Roediger J. C., Courteau S., 2015, *MNRAS*, **452**, 3209
 Rubin V. C., Burstein D., Ford Jr. W. K., Thonnard N., 1985, *ApJ*, **289**, 81
 Saintonge A., et al., 2011, *MNRAS*, **415**, 32

- Sales L. V., et al., 2017, *MNRAS*, **464**, 2419
 Schaye J., et al., 2015, *MNRAS*, **446**, 521
 Schombert J., McGaugh S., 2014, *Publ. Astron. Soc. Australia*, **31**, e036
 Shapiro K. L., et al., 2010, *MNRAS*, **402**, 2140
 Sorce J. G., Guo Q., 2016, *MNRAS*, **458**, 2667
 Sorce J. G., et al., 2013, *ApJ*, **765**, 94
 Trujillo-Gomez S., Klypin A., Primack J., Romanowsky A. J., 2011, *ApJ*, **742**, 16
 Tully R. B., Courtois H. M., 2012, *ApJ*, **749**, 78
 Tully R. B., Fisher J. R., 1977, *A&A*, **54**, 661
 Verbeke R., Vandenbroucke B., De Rijcke S., 2015, *ApJ*, **815**, 85
 Verheijen M. A. W., 2001, *ApJ*, **563**, 694
 Vogelsberger M., et al., 2014, *MNRAS*, **444**, 1518
 Westfall K. B., Bershady M. A., Verheijen M. A. W., Andersen D. R., Martinsson T. P. K., Swaters R. A., Schechtman-Rook A., 2011, *ApJ*, **742**, 18
 Wright E. L., et al., 2010, *AJ*, **140**, 1868
 Young J. S., Scoville N. Z., 1991, *ARA&A*, **29**, 581
 Zaritsky D., et al., 2014, *AJ*, **147**, 134
 da Cunha E., Charlot S., Elbaz D., 2008, *MNRAS*, **388**, 1595
 de Grijs R., van der Kruit P. C., 1996, *A&AS*, **117**, 19
 van den Bosch F. C., 2000, *ApJ*, **530**, 177
 van der Kruit P. C., Searle L., 1981, *A&A*, **95**, 105

APPENDIX A: UNCERTAINTIES IN THE SED-FITTING

It is clearly demonstrated in Figures 7 and 8 that $3.6 \mu\text{m}$ stellar mass-to-light ratios, measured from the SED-fitting span a wide range, while stellar population synthesis models predict this value to be more or less constant. The major concern regarding the SED-fitting results is that for several objects mass-to-light ratios are very small, for example $\Upsilon_{\star}^{SED,[3.6]} = 0.03$ for IC2574 or $\Upsilon_{\star}^{SED,[3.6]} = 0.04$ for NGC 2366. If these were real, the galaxies would produce 10 times more light for the same mass, and this should be seen strongly in the colours, unless most of it is obscured. Figures A1 and A2 show the correlation between $\Upsilon_{\star}^{SED,[3.6]}$ and $g-r$ colour and total luminosity of a galaxy in the $3.6 \mu\text{m}$ band ($L_{[3.6]}$), respectively. While the correlation between $\Upsilon_{\star}^{SED,[3.6]}$ and $g-r$ colour is absent with Pearson's coefficient r equal to 0.37, $\Upsilon_{\star}^{SED,[3.6]}$ correlates well with the $L_{[3.6]}$ ($r = 0.66$). This correlation with the band which is closely related to the stellar mass illustrates that mostly low mass dwarf galaxies have low mass-to-light ratios. The possible reason is the fact that there might be contamination of the $3.6 \mu\text{m}$ flux due to non-stellar emission and by the leakage of the PAH bands. However, the low mass-to-light ratios of these galaxies do not directly result into an increased scatter of the BTFR, as many of them have rising rotation curves and were not included in the statistical analysis.

Another concern is that the best errors we can apply to the stellar mass-to-light resulting from the SED-fitting are motivated by the study of Roediger & Courteau (2015) who found a very low error of 0.1 dex using a set of simulated galaxies. However, Roediger & Courteau (2015) only used *griz* and *H*-band for their study, basically only bands dominated by the stars. Unlike us, they did not use any dust emission. The inclusion of the dust emission is an important constraint as it regulates the amount of extinction in the

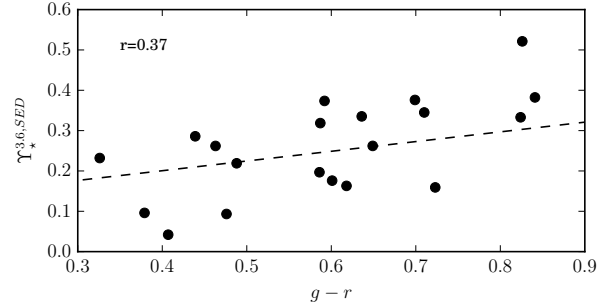


Figure A1. Correlation between $\Upsilon_{\star}^{SED,[3.6]}$ and $g-r$ colour. r is Pearson's correlation coefficient.

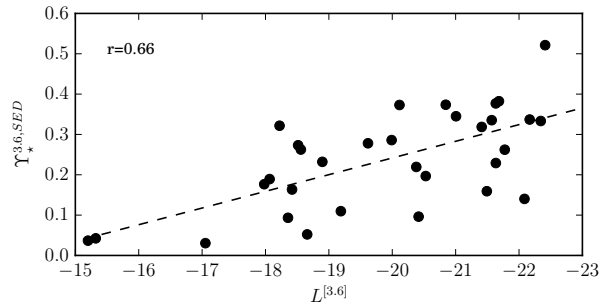


Figure A2. Correlation between $\Upsilon_{\star}^{SED,[3.6]}$ and total luminosity of a galaxy in $3.6 \mu\text{m}$ band. r is Pearson's correlation coefficient.

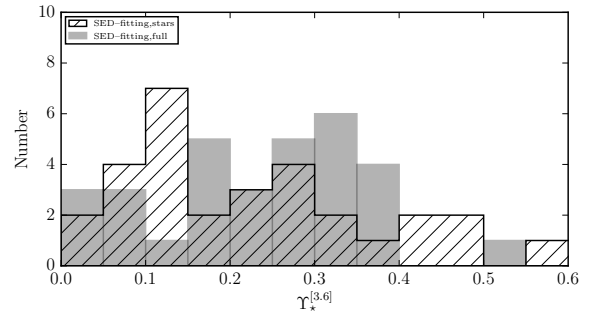


Figure A3. A comparison between $\Upsilon_{\star}^{SED,[3.6]}$ obtained using information from all 18 bands (grey area) and using only stellar bands *griz* & *JH* (hatched area).

bands dominated by stellar light. Figure A3 shows a comparison between $\Upsilon_{\star}^{SED,[3.6]}$ obtained using information from all 18 bands and using only the stellar *griz* & *JHK* bands, similar to Roediger & Courteau (2015). It is clearly seen from Figure A3 that use of only stellar bands still produces a wide spread of $\Upsilon_{\star}^{SED,[3.6]}$. Moreover, the amount of galaxies with very low mass-to-light ratios increases. Figure A4 shows the correlation ($r = 0.63$) between the difference of fluxes in the *z*- and *J*-bands and the minimum χ^2 for the best-fit SED-fitting model for each galaxy. The correlation between other bands flux ratios and χ^2 is absent.

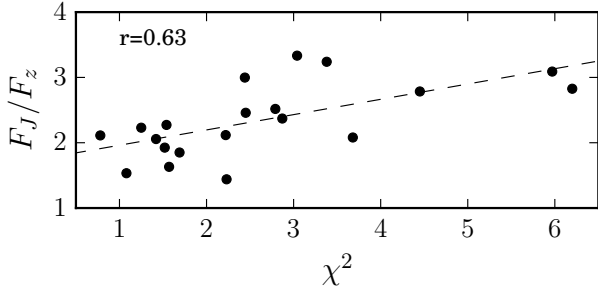


Figure A4. Correlation between the difference of fluxes in z - and J - bands and the minimum χ^2 for the best-fit SED-fitting model. r is Pearson's correlation coefficient.

APPENDIX B: SED BEST-FIT MODELS FOR OUR SAMPLE GALAXIES

In Figures B1– B32 we present the best-fit models performed with MAGPHYS (in black) over the observed spectral energy distribution of our sample galaxies (see Figure 4 for an example). The blue curve shows the unattenuated stellar population spectrum. The bottom plot shows the residuals for each measurement $((L_{obs} - L_{mod})/L_{obs})$. The full Appendix B data can be found [here](#).